Damage Assessment in TiB_2 Ceramic Armor Targets

Nevin L. Rupert, William H. Green, Joseph M. Wells, and
Kevin J. Doherty

20011231 152

Army Research Laboratory

Aberdeen Proving Ground, MD 21005-5066

Damage Assessment in TiB$_2$ Ceramic Armor Targets

Nevin L. Rupert, William H. Green, Joseph M. Wells, and
Kevin J. Doherty
Weapons and Materials Research Directorate, ARL

Abstract

The interaction between long rods and ceramics is only partially understood; however, this understanding is essential in the design of improved performance of impact-resistant materials and armor system design applications. The current work takes a preliminary look into the modern mythology surrounding the formation of radial cracking in ceramics during ballistic penetration. Tests were conducted using a 32-g tungsten alloy laboratory penetrator with a length to diameter ratio (L/D) = 20 at a nominal impact velocity of 1,600 m/s. Testing evaluated both prestressed and unstressed titanium diboride (TiB_2) ceramic tiles. Evaluation of the damage included microstructural analysis using a scanning electron microscope (SEM) with a Robinson backscatter detector for surface structure, the x-ray computed tomography (CT) nondestructive technique to completely scan the interior of each disk, and limited analytical modeling of the stress state.

Acknowledgments

INTENTIONALLY LEFT BLANK.

Contents

List of Figures

List of Tables

INTENTIONALLY LEFT BLANK.

1. Introduction

Of recent interest within the ceramic armor community has been the possibility of an interface-defeat-based ceramic armor. The interface-defeat phenomenon has been demonstrated convincingly by Hauver et al. (1993; 1994) with highly constrained ceramic tiles. Such armor designs are based on the interfacial flow of the penetrator material at the surface of the ceramic with minimal penetration. Grace (1997) proposed a shear failure mechanism in the ceramics interface target designs that terminates interface defeat. His suggestion is supported by the work of Lundberg et al. (2000). The present study is a preliminary look at the radial cracking that occurs within the ceramic tiles from interface-defeat-based armor targets after ceramic penetration initiates.

Post-mortems of three interface-defeat-based targets were evaluated using scanning electron microscopy (SEM) and microchemical analysis for examination of the ceramic fracture morphology. X-ray computed tomography (CT) (Stanley 1985; Dennis 1989) was used to provide accurate nondestructive visualization of the mesodamage within selected opaque target components. Further analysis of the ceramic disk is based on the damage assessment presented by the x-ray CT scans to define crack lengths and boundary placements coupled with a stress analysis based on the work of Lamé (1852) and Irwin et al. (1958) to determine the state of prestress and defining the minimum internal pressure generated by the penetration process to initiate radial cracking.

2. Setup and Ballistic Test Procedures

Two target designs were evaluated using the U.S. Army Research Laboratory (ARL) Light Gas Gun Facility. The target construction followed general features of the standard design, as shown in Figure 1 (Hauver to be published). The 38-mm × 38-mm attenuator consisted of 15 layers of 0.50-mm 1100 aluminum evenly interspersed among 16 layers of 0.58-mm polyethylene. The attenuator was then bonded to the 25.4-mm titanium alloy (Ti/6% Al/4% V) cover plate. A 2.39-mm-deep × 82.55-mm-diameter recess was cut into the rear surface of the cover plate and completely filled with a graphite disk. Variations in the general target design were then introduced by changing the diameter and lateral confinement conditions for the ceramic insert. A pocket was machined in the rear titanium alloy plate to within 31.75 mm of the rear surface. After the ceramic is inserted in the rear plate, the front face is then machined flush with the

top surface of the ceramic insert. The two titanium plates are then peripherally welded together.

The 72-mm-diameter ceramic disks used in the target designs were cut from a single high-purity armor-grade TiB_2 tile manufactured by CERCOM, Inc.[*] The tile was 25 mm thick. Nominal properties as advertised by CERCOM for the ceramic are:

- Density   4.48 g/cm^3,

- Hardness — Knoop 300-g scale   2,700 kg/mm^2,

- Average grain size   15 μm,

- Compressive strength   4.82 GPa, and

- Fracture toughness (K_{Ic})   6.95 $MPa(m)^{1/2}$.

The first ceramic insert design consisted of a double shrink fit. First, a cylinder of 17-4PH steel was placed around the 72-mm ceramic disk which resulted in the initial prestress of the ceramic insert. These assemblies were then placed into a titanium body with an interference fit. The interference between the titanium body, steel ring, and ceramic disk resulted in a nominal calculated compressive pressure of 128 MPa in the TiB_2 disk. The second design eliminated the double shrink fit in the general target design by directly potting the ceramic insert into the titanium body. This arrangement resulted in lateral confinement of the ceramic without prestressing it.

Both target designs were then impacted at 1,600 m/s (nominal) by tungsten heavy alloy (WHA) hemispherical-nose long rod (L/D = 20) penetrators manufactured by Teledyne Firth Sterling using the X-21C process with approximately 25% swagging. One target using the prestressed ceramic design was impacted a second time after replacing the attenuator. Ballistic results of all tests are listed in Table 1.

The penetrators used in this study were manufactured with a diameter of 4.93 mm and a mass of 32.5 g. The WHA had a nominal alloy composition of 93% W/4.9% Ni/2.1% Fe. Nominal properties for the penetrators are:

- Density (Dowding 1999; Teledyne Firth Sterling 1991)   17.73 g/cm^3,

- Hardness — Rockwell C Scale (Dowding 1999; Teledyne Firth Sterling 1991)   40.5–42.6,

---

[*] CERCOM, Inc., 1960 Watson Way, Vista, CA 92083.

Table 1. Experimental results.

Test Number	Ceramic Diameter[a]	Impact Velocity	DOP[b] into Ti Plate
340	72 mm/w	1,589 m/s	4.0 mm[c]
R-1	72 mm/w	1,600 m/s	10.9 mm[c]
R-1(2nd)	72 mm/w	1,594 m/s	10.0 mm
R-2	72 mm	1,597 m/s	d
R-7	72 mm	1,587 m/s	7.4 mm

[a] /w = with shrink fitted 17-4 PH steel ring.
[b] DOP = depth of penetration.
[c] DOP into TiB_2.
[d] Complete penetration; DOP not measured.

- Yield strength (Dowding 1999; Teledyne Firth Sterling 1991)   1.09–1.17 GPa,

- Ultimate strength (Dowding 1999; Teledyne Firth Sterling 1991)   1.13–1.21 GPa,

- Elongation (Dowding 1999; Teledyne Firth Sterling 1991)   5.8–10.6%.

3. Evaluation of Target Disks

3.1 Macro Scale Visual Inspection

Macro photographs of the three ceramic disk targets after impact are shown in Figures 2, 3, and 4. Figure 2 shows a confined, but not prestressed, target disk. Figures 3 and 4 show prestressed disks using the 17-4PH steel rings for compression, with Figure 3 showing the result of one ballistic impact and Figure 4 showing the result of two sequential impacts. Figure 2 illustrates the typical appearance of a ceramic target when interface flow does not completely erode the penetrator. Initial inspection of the target after the cover plate was removed showed a mixture of residual penetrator material and powdered ceramic adhering to the cover plate. The mixture covered an area approximately 25 mm in diameter and was about 7 mm thick. The remaining ceramic, shown in Figure 2, has a hole perforating the center of the disk, a region of comminuted ceramic surrounding the hole, and extensive radial cracking reaching the outer edges of the disk. Contrast this with the appearance of the ceramic disk in Figure 3, where the penetrator was defeated, which shows very little radial cracking. The penetrator in this disk reached a depth of approximately 11 mm.

The ceramic disk in Figure 4, which was completely penetrated by the second impact, has similarities to the disk in Figure 2.

3.2 Micro Scale Evaluation

SEM and microchemical analysis for examination of the ceramic fracture morphology is discussed here mainly because they were done on as-impacted (i.e., not sectioned) disks, since each disk was subsequently examined using the state-of-the-art x-ray CT nondestructive evaluation technique. Figures 5 and 6 show representative impact surface structures of the prestressed disks shown in Figures 3 (one impact) and 4 (two impacts), respectively. The images show similar fracture surfaces. However, the sequentially impacted surface in Figure 6 shows a much larger amount of rubble (comminuted TiB_2) than in the single impact disk. This rubble is on the order of tens of microns in size and is adhered to the disk surface.

A Robinson backscatter detector on the SEM was used to image residual penetrator material on the surface of the sequentially impacted disk. This method shows heavier elements such as tungsten as a lighter shade of gray or white. In Figure 7, which is a low magnification image, a region of tungsten (shown as lighter gray or white) lies to the left of the hole (shown as darker gray or black) from the second impact. At higher magnifications, as shown in Figures 8 and 9, the tungsten region can be identified as individual particles ranging in size from submicron to tens of microns that are intermixed with particles of the ceramic spread on the surface of the disk.

SEM images from the sequentially impacted disk also show a significant amount of comminuted ceramic adhered to the surface of the disk. Figure 10 was taken closer to the overall impact zone and shows a higher number of smaller pieces of comminuted ceramic. Figure 11, taken at increased distance from the impact zone, shows fewer smaller pieces as well as some relatively larger pieces of comminuted ceramic.

3.3 Meso Scale Evaluation Using X-ray CT

The SEM is an adequate tool to characterize the many features associated with the impact surfaces of the ceramic disks, but it cannot provide any information about the damage within the body of the disks. An overview of the principles and technique of x-ray CT as well as a description of three-dimensional (3-D) volume reconstruction from multiple CT slices (i.e., scans) and subsequent generation of 3-D point clouds may be found in Wells et al. (2001).

3.3.1 X-ray CT Method

3.3.1.1 Principles and Technique

Figure 12 schematically shows the rotate-only (RO) x-ray CT technique. The x-ray source and detector remain stationary. The object remains stationary relative to the turntable. The collimated horizontal fan beam "scans" a slice of the object, as the turntable rotates 360°. The height above the turntable and thickness of the slice are known. A set of attenuation line integrals is generated from the scan. The line integrals can be conceptually grouped into subsets referred to as "views." Each view corresponds to a set of ray paths through the object from a particular direction. The views are also referred to as "projections" or "profiles," while each individual datum within a given projection is referred to as a "sample" or often just a "data point."

A state-of-the-art scanner routinely collects millions of measurements per scan, each one accurately quantified and precisely referenced to a specific line of sight through the object of interest. The views from the scan are passed to the reconstruction algorithm for processing (Stanley 1985). The CT reconstruction process yields a two-dimensional (2-D) array of numbers corresponding to the cross section of the object. This 2-D array of numbers (i.e., densitometric gray levels) is the CT image.

3.3.1.2 3-D Volume Reconstruction

The spatial precision and digital nature of CT images allow for the accurate volume reconstruction of multiple adjacent slices. The slices are "stacked" to provide 3-D information throughout the entire object or a section of the object. Two ways of visualizing volumetric data are multiplanar reconstruction (MPR) and 3-D reconstruction. MPR (visualization) displays top, front, side, and oblique slices through the object. The orientation of the top slice is parallel to the cross-sectional image plane. The front slice is orthogonal to the top slice. The side slice is orthogonal to both the top and front slices. The oblique slice can be placed on any one of the other three slices. The MPR display is similar to an engineering drawing. However, each view (i.e., top, front, side, and oblique) is a slice with finite thickness through the object, not a 2-D projection. The top, front, and side slices can be moved anywhere in the reconstructed volume. The oblique slice can be rotated through 360°. The volumetric data is displayed as a 3-D solid object in 3-D reconstruction, and the orientation of the solid in space can be changed to facilitate different views. The solid can also be "virtually" sectioned by only displaying part of the reconstructed volume, which creates a "virtual" cutting plane on the solid showing the x-ray density values on that plane. This plane may be orthogonal to the cross-sectional image plane. In effect, virtual sectioning shows the exposed surface as it would look if the object were actually destructively sectioned along that plane.

3.3.1.3 3-D Point Cloud Generation

As previously stated, a CT image is a 2-D array of densitometric gray levels (i.e., CT densities). For example, a 12-bit image would have 4,096 levels of gray from black to white, with darker (blacker) normally indicating less x-ray attenuation and lighter (whiter) indicating more attenuation. The field of image processing is too great to discuss in detail here, but it is sufficient to state that different materials in an image can be visually delineated to a high degree using various image processing techniques based upon their attenuation characteristics. In fact, black (gray level = 0) and white (gray level = 4,095) images can be generated using appropriate contrast enhancement. This is normally done to accurately define material (white) boundaries. Any number of black and white (i.e., binary) images can be vertically stacked to generate a 3-D point cloud, in which the set of points in space defines the internal and external surfaces of the object. Furthermore, a point cloud can be "polygonized" or made into a wireform model.

3.3.1.4 Resolution

Table 2 lists approximate resolutions achieved for different modes of image visualization.

Table 2. Approximate resolutions achieved for different modes of image visualization.

Visualization Mode	View Description	Image Spatial Resolution
2-D CT Slice	Traditional cross-section plane orthogonal to vertical axis	$\approx$400 μm
MPR Pseudo 3-D	Arbitrary multiplanar slices	$\approx$400 μm
3-D Solid (with or without cut sections)	Oblique view showing cracks within base material	$\approx$400 μm
3-D Point Cloud (polygon/wireform model)	3-D view of crack network only with base material removed	$\approx$400 μm ($\approx$500 μm in the Z-direction)[a]

[a] Assumes point cloud not significantly undersampled.

3.3.2 CT Equipment

The TiB_2 disks were examined using a customized ACTIS 600/420 CT system designed and constructed by Bio-Imaging Research (BIR), Inc. and installed at ARL at Aberdeen Proving Ground, MD. It has a 420 keV x-ray tube with two focal spot sizes and a 160 keV microfocus x-ray tube with four focal spot sizes, the smallest being 10 μm. It also has a linear detector array (LDA) and an image intensifier (II) with a zoom lens and a charged-coupled device camera. CT

6

scanning can be done using the LDA or the II. The system can scan in RO and offset-RO mode using either source and the LDA or the II, and in translate-rotate (TR) mode using the LDA and either source. It can also perform digital radiography (DR) scans using the LDA or II.

3.3.3 CT Technique

The entire thickness of each TiB$_2$ disk was scanned parallel to their impact faces in RO mode with their impact faces facing up. The prestressed disks remained within their 17-4PH steel compression rings. The confined-only disk remained within a sectioned block of titanium to maintain its integrity. The source-to-object distance and source-to-image distance were 747.6 mm and 928.0 mm, respectively. The slice thickness and increment were 0.50 mm and 0.50 mm, respectively, resulting in contiguous scans. The scan configuration used the 420 keV tube with the LDA. The tube energy and current used were 415 keV and 2.0 mA, respectively, and the focal spot was 0.8 mm.

The sequentially impacted prestressed disk was also scanned perpendicular to the impact face in two different positions to better locate and resolve radial cracking through the thickness of the disk, since very high attenuating residual penetrator material is generally not near the edges of the disk. In this orientation, the impact face is vertical and perpendicular to the horizontal x-ray fan beam. The effect of relatively large amounts of residual penetrator material in CT images is discussed later in this report. A series of perpendicular scans were made near the edges without scanning through residual penetrator material. These scans were examined using MPR (Wells et al. 2001), to volumetrically reconstruct CT slices parallel to the impact face showing material from the edge of the disk to the extent of the perpendicular scans. Thus, only part of the area of the disk is shown in the MPR images, as opposed to the entire area over the diameter. Except for the slice thickness and increment in the perpendicular scan data set, which were 0.50 mm and 0.25 mm, respectively, the technique parameters were the same as the parallel scan data set. Overlapping scans, as these were, generally improve MPR and 3-D solid images because they result in better quality attenuation data (i.e., better photon statistics) in the overlapping regions.

3.3.4 Confined Disk With One Impact

Figure 13 is a flash radiograph of a long rod penetrator as it is in the process of perforating a TiB$_2$ ceramic disk. This radiograph illustrates the presence of a limited initial lateral flow of the penetrator material on the ceramic surface prior to penetrating the disk. A CT scan 21.0 mm from the impact face is shown in Figure 14. The extent of the diameter of the disk is within the black ring. A flower petal-like pattern of dark band delimited ceramic damage is evident near the outside edges of the disk. Figure 14 also shows the presence of residual

penetrator material (debris) shown in white. It should be noted that highly attenuating material like the tungsten penetrator causes some streaking in the image around it. This streaking is an image artifact and is not indicative of any real physical changes in the state of the material. Figure 15 is a CT scan 4.5 mm from the impact face showing approximately the depth at which outer radial cracking begins. The circumferential/laminar damage is more complicated closer to the impact face. Figure 16 is a CT scan 3.0 mm from the impact face showing two outer radial cracks in the top area of the image. It should be noted that the cracks are wider at the edges of the disk and thinner towards the center of the disk. Figure 17 is a CT scan only 1.0 mm from the impact face showing how the outer radial cracks become longer closer to the impact face. Figures 16 and 17 also show relatively short cracks originating in areas of comminuted ceramic damage. These types of cracks are more difficult to identify in these images due to their close proximity to highly attenuating residual penetrator material.

Figure 18 is an MPR image showing two perpendicular slices to the top slice view (top left), which is parallel to the CT scan plane. The top slice view passes through the midplane of the disk. The front slice (bottom) and side slice (top right) views are orthogonal 25-mm-thick slices in the through-thickness direction of the disk, which, in this case, pass through the approximate center of the disk. The MPR image shows the cracking and comminuted damage, as well as the non-uniform columnar placement of residual penetrator material, within the disk in these views. In general, the three different views can be arbitrarily located anywhere within the disk.

Figure 19(a) is a 3-D solid image of the entire disk with the impact face at the top of the image. Figure 19(b) is a 3-D solid image of the disk with approximately half of it "virtually" cut off perpendicular to the impact face (i.e., a semicircular section). This image shows damage and residual penetrator material in the virtual sectioned face. That is, if the disk were actually physically sectioned at the virtual location the revealed surface would have the damage and residual penetrator material as shown in Figure 19(b), assuming the sectioning process did not obscure or destroy it. Figure 19(c) is a further sectioned 3-D solid image showing only 1/4 of the entire disk.

As seen in Figures 14–18, the location of the white residual penetrator material is very evident. However, it is desirable to know the 3-D distribution of the material to determine its depth and lateral extent, or spread, in the disk, and to determine the degree to which the penetrator was broken up in the disk during impact. This type of information is useful in understanding the interaction between the penetrator and the target. Figure 20(a) is a 3-D point cloud looking in the through-thickness direction which defines the boundary locations of the residual penetrator material within the disk (it is upside down relative to Figure 15). The x-direction is to the left and the z-direction is into the page. In

Figure 20(b), the x-direction is still to the left, but the z-direction is rotated 25° counterclockwise (i.e., out of the page) from vertical about the x-axis. The z-direction relative to the disk is from the rear face to the impact face. Therefore, the point cloud is oriented such that the impact face, which is physically at the top of the image, is being viewed obliquely. An outline of the impact and rear face edges of the disk are superimposed in these figures to reference the true location and orientation of the residual penetrator material point cloud. The "front" edge of the rear face is physically at the bottom of the image and the dashed "back" edge of the rear face is physically behind the point cloud. BIR ACTIS software was used to perform line profiling, create binary images, and generate the point cloud data. A general description of how to create binary images using line profile data is hereby described (Wells et al. 2001):

- The first step in obtaining the point cloud is to perform the required image processing to "clean up" undesirable image features or artifacts. This step may be simple or complicated, depending on image quality.

- The next step is to determine the best gray level to use to threshold and binarize the images (i.e., show only two gray levels or black and white). This is done by "line profiling" the feature(s) of interest in the image. Normally, the full-width-half-maximum value, which is the gray level half way between the minimum and maximums of the profile, is used. The result of binarizing the image is based on the profile. A number of binary images are then volumetrically combined to generate a 3-D point cloud describing "boundaries" of the cracking damage and comminuted ceramic material.

- A systematic sampling technique is then applied to decrease the amount of data and make the point cloud more visually informative, since the point cloud contained more points than were necessary for data analysis. BIR ACTIS software was used to perform the line profiling, create binary images, and generate point cloud data. SURFACER software by SDRC/Imageware, Inc., was used to visualize the point cloud data. It is apparent from the point cloud that residual penetrator material is present through the thickness of the disk with approximately uniform lateral extent.

3.3.5 Confined and Prestressed Disk With One Impact

Figure 21 shows a static post-mortem flash radiograph of the residual penetrator material within the disk, in which the presence of extensive lateral flow of penetrator material is evident. A CT scan 22.5 mm from the impact face is shown in Figure 22. The extent of the diameter of the disk is within the black (on the left) and white (on the right) ring. Figure 22 shows that the disk has excellent physical integrity at this depth location, which is representative of the CT scans beneath the impact crater. Figure 23 is a CT scan 3.0 mm from the impact face

exhibiting no radial cracking, some fractured ceramic above the crater, and very little residual penetrator material within the crater. The disk material outside of the crater is largely intact, except for the relatively small band of fractured ceramic. Again, these characteristics are representative of the disk in the CT slices containing the crater.

3.3.6 Confined and Prestressed Disk with Two Impacts

Figure 24 shows a static post-mortem flash radiograph of the second impact into the ceramic disk shown in Figure 22 (section 3.3.5). Additional lateral flow of the penetrator material is not evident when compared with Figure 21. A CT scan 23.5 mm from the impact face is shown in Figure 25. Figure 26 shows a CT scan 3.5 mm from the impact face with significantly more residual penetrator material, which has the effect of obscuring relatively small radial cracking, especially internal cracking, due to the streaking artifact. Figure 27(a) is a 3-D point cloud looking in the through-thickness direction of the combined residual penetrator material left in the disk after both impacts (it is upside down relative to Figure 25). In Figure 27(b), the orientation of the point cloud is the same as in Figure 20(b). The bimodal distribution of the combined residual penetrator material is evident in Figure 27(b) and the material is widely dispersed. The "partial cloud" more towards the center of the disk with greater depth is from the second impact, which perforated the rear face of the disk. Radial cracking is heavily masked in the CT scan in Figure 26 because of the residual penetrator material. Consequently, the disk was scanned perpendicular to the impact face as discussed in section 3.3.3 and MPR images were reconstructed from these scans. Figures 28(a)-(c) are such images, in which only the top slice view (top of image) parallel to the scan plane and front slice view (bottom of image) parallel to the impact face are shown. The front slice view passes through the top slice view perpendicular to the page. In Figure 28(a), the top slice is located near the top edge of the disk as it rested on its side on the (scanning) turntable and the front slice (FS) is 0.97 mm from the impact face, which is at the top of the top slice view. In Figures 28(b) and (c), the top slice is at the same location as in Figure 28(a), but the front slice is 2.15 mm and 3.32 mm from the impact face, respectively. The white material in Figures 28(a)-(c) is the steel constraining ring. At a depth of about 3 mm, the outer radial cracks are less visible and circumferential/laminar cracks appear. The radial cracks in the front slice views are not as long as those in the once-impacted confined-only disk (section 3.3.4). Secondly, these cracks change in size relatively little as a function of depth compared to those in the confined-only disk and they are relatively shallow, having a depth of only about 2 mm.

4. Analysis of Target (Solid Mechanics)

Current modeling of ceramics is based on strain energy release rates (Rupert et al. 2001). They assume that the formation of radial cracks within the ceramic is the result of internal pressurization of the penetration cavity. To calculate the stresses, strains, and strain energy within the ceramic disk as a result of the prestressing from the double shrink fit and the pressurization of the cavity during penetration, the target was analyzed as a series of thick cylinders subjected to external and internal uniformly distributed pressures as described by Lamé (1852) for a fixed cylinder length. The schematic of a cylinder of length l, internal radius r_1, and external radius r_2, subjected to internal and external uniformly distributed pressures p_1 and p_2, is shown in Figure 29.

The strains will be expressed by equation 1:

$$\epsilon_r = \frac{1}{E}\left[(1 - v^2)\sigma_r - v(1 + v)\sigma_\theta\right],$$

$$\epsilon_\theta = \frac{1}{E}\left[(1 - v^2)\sigma_\theta - v(1 + v)\sigma_r\right], \tag{1}$$

$$\epsilon_z = -\frac{2v\left(r_1^2 p_1 - r_2^2 p_2\right)}{E\left(r_2^2 - r_1^2\right)}.$$

The stresses will be expressed by equation 2:

$$\sigma_r = \frac{r_1^2 r_2^2 \left(p_2 - p_1\right)}{r_2^2 - r_1^2}\frac{1}{r^2} + \frac{r_1^2 p_1 - r_2^2 p_2}{r_2^2 - r_1^2},$$

$$\sigma_\theta = \frac{r_1^2 r_2^2 \left(p_2 - p_1\right)}{r_2^2 - r_1^2}\frac{1}{r^2} + \frac{r_1^2 p_1 - r_2^2 p_2}{r_2^2 - r_1^2}, \tag{2}$$

$$\sigma_z = \frac{2v\left(r_1^2 p_1 - r_2^2 p_2\right)}{r_2^2 - r_1^2} = \text{constant}.$$

These equations are identical to those as derived by Lamé (1852) for a fixed cylinder length except for σ_z and ϵ_z, which were derived for a cylinder where the ends are free (Volterra and Gains 1971).

Setting the external radius of the titanium target holder to infinity ($r_2 = \infty$ for Ti plate) and the internal radius of the ceramic disk to zero ($r_1 = 0$ for TiB$_2$ disk), an internal stress of 128 MPa was calculated for the disk as a result of balancing the

pressures at the interfaces and accounting for the interferences between the ceramic disk, steel ring, and titanium plate forming the double shrink fit used in the target construction. This compares quite favorably with the measured prestress of 137 MPa of a silicon carbide (SiC) disk of the same overall target general design and construction tolerances (Trevino et al. 1998).

To estimate the stress state in the elastic portion of the disk during penetration, certain assumptions are made. First, the comminuted ceramic has no shear strength and acts like fluid pressurizing the internal surface of the ceramic cylinder. Second, the minimum hoop stress, σ_θ, required to initiate radial cracking is related to the fracture toughness of the ceramic. This minimum hoop stress for fracture is expressed by equation 3:

$$\sigma_o \equiv \sigma_\theta = \frac{K_{Ic}}{2(\pi a)^{\frac{1}{2}}} \ . \tag{3}$$

K_{Ic} is defined as the ceramic's mode I fracture toughness, a is the initial crack size, and σ_θ is the hoop stress at the comminuted/intact ceramic interface representing the phenomenological yield stress of the ceramic σ_n (Irwin et al. 1958).

Defining the initial crack length at the comminuted/intact interface as one grain diameter (17 μm), equation 3 was then used to define the minimum hoop stress required to initiate the formation of radial cracks outward from the interface. This was then coupled with equations 1 and 2 to balance the forces and displacements at the interfaces for the double shrink-fit on the ceramic disk to determine the pressure profiles presented in Figures 30 and 31. For the titanium block, r_2 was set to infinity in these calculations. Figure 30 plots the necessary pressure resulting from the penetration process to initiate radial cracking as 100%. Internal pressures required to generate 15%, 30%, and 45% overpressures in hoop stress that may result from the penetration process are also presented for comparison. Figure 31 proffers the corresponding pressures applied at the outer edge of the ceramic disk.

Upon acquiring the pressure profiles for the ceramic disk, determination of the radius for zero hoop stress could be made. The radius at which zero hoop stress occurs is expressed by equation 4:

$$r_{zero} = \left(\frac{r_1^2 r_2^2 (p_2 - p_1)}{r_1^2 p_1 - r_2^2 p_2} \right)^{\frac{1}{2}} \ . \tag{4}$$

The difference between the zero hoop stress radius and the comminuted/intact interface radius can then be used to predict the maximum radial crack length resulting from internal pressurization of the ceramic disk. Figure 32 shows the

plot for the minimum pressure curve for fracture and three additional overpressure curves. In Figure 32, all four crack length curves are superimposed upon each other, inferring that increased pressure from the penetration process does not result in increased radial crack length. Therefore, to offset the increases in strain energy resulting from the increased internal pressure the number of radial cracks formed will have to increase proportionally with the strain energy. Figure 32 also defines a maximum crack length of 10.5 mm which occurs at a comminuted/intact ceramic interface radius of 25.5 mm. This corresponds to the zero hoop stress occurring at the ceramic/steel ring interface.

In an effort to determine the cause of the second set of radial cracks which originates at the outer surface of the ceramic disk, strain energy calculations were made assuming the minimum internal pressure to initiate cracking as given by equation 3. Shear stresses, τ_θ and τ_r, within the cylinder are set to zero as a result of the symmetry of the problem. The strain energy is expressed by equation 5:

$$ U = \frac{1}{2} \int_V \sigma_r \epsilon_r + \sigma_\theta \epsilon_\theta + \sigma_z \epsilon_z dV . \tag{5} $$

The stresses and strains used in equation 5 are defined by equations 1 and 2.

Figure 33 provides a plot of the total strain energy as a function of radius for six different comminuted/intact ceramic interface radiuses. These plots illustrate that the strain energy density resulting from the double shrink fits and internal pressurization of the ceramic disk during penetration is insufficient to cause the formation of the second radial crack pattern observed by Green et al. (2001). An alternative explanation for the formation of these radial cracks is a reflected release wave off the ceramic/steel ring (or adhesive) interface. Additional work will be done to estimate the magnitude of the release wave required to initiate cracking in the ceramic and the resulting strain energy distribution.

A second observation was made based on the strain energy calculations. The comminuted/intact ceramic interface radius experimentally measured by Green et al. (2001) for both the prestressed and unstressed ceramic disk coincides with the radius which results in maximum strain energy stored within the ceramic disk. Due to the limited data available at this time, additional testing will be required to verify the existence of any relationship between the penetration cavity diameter and maximum strain energy remaining within the intact ceramic. The authors are currently pursuing the experimental and analytical verification of the existence of such a relationship.

5. Summary and Conclusions

The results of SEM microstructural and x-ray CT mesostructural (10^2 μm–10^3 μm) analyses of three ballistically impacted TiB$_2$ ceramic disks were presented. The SEM analysis studied the ceramic surface fracture morphology of the disks. The CT evaluation successfully located the ballistic impact damage and residual penetrator material within the entire volume of each disk. Destructive sectioning would provide additional information on the impact damage and residual penetrator material within the ceramic disk on the micro scale. However, the time and resources needed to complete a destructive sectioning of one of the disks used in this study were not available. The University of Texas at El Paso was provided three of the ceramic disks used in this study for their own microstructural evaluations. Results from these examinations will be published in a subsequent report.

The first disk, which was not prestressed using the 17-4PH stainless steel constraining ring, was completely penetrated by the single impact. There was extensive ballistic damage within the disk, including comminuted ceramic damage and both internal and outer radial cracking. The internal cracking originated from areas of comminuted damage and the outer cracking originated from the edges (i.e., the circumference) of the disk. The outer radial cracking was unanticipated and is contrary to current damage models. The CT slices through the disk also showed the presence of complicated banded circumferential damage. The residual penetrator material was dispersed through the thickness of the disk with approximately uniform lateral extent (i.e., columnar).

The second disk, which was prestressed, was impacted one time and exhibited extensive lateral flow of penetrator material. The penetrator reached a depth of approximately 11 mm and there was very little damage within the disk excluding the impact crater, including considerably reduced radial cracking. The differences in impact damage in this disk compared to the first disk (confined-only) can be attributed mainly to the compressive prestress resulting from the constraining ring.

The third disk, which was also prestressed, was impacted two times with the attenuator being replaced between impacts and the disk was completely penetrated by the second impact. There was extensive ballistic damage within the disk similar to that within the single impacted confined-only disk, including comminuted ceramic damage and both internal and outer radial cracking. Internal cracking was difficult to identify in the CT slices because of the relatively large amount of combined residual penetrator material present. As was the case with the single impacted confined-only disk, the CT slices also showed the presence of banded circumferential damage. Secondly, a portion of the

14

combined residual penetrator material is dispersed through most of the thickness of the disk near its center, which resulted from the second impact. However, the combined material as a whole is widely laterally dispersed and has a bimodal distribution.

The comparison of detailed and accurately (volumetrically) located ballistic impact damage and residual penetrator material in the three disks was important in gaining a better understanding of the penetrator-ceramic interaction in these ballistic test cases. The authors will continue to apply x-ray CT evaluation in future work on improved impact-resistant materials, including interface-defeat-based ceramic armor, and are excited about the potential for better understanding of the penetrator-ceramic interaction using extensive knowledge of the ballistic impact damage obtained by x-ray CT. Work in the near future will address the removal of the penetrator material (digitally) from the scan to facilitate the mapping of the ceramic damage.

Two sets of radial cracks were observed from the x-ray CT scans of the ceramic disks. These included one set that originated at the comminuted/intact ceramic interface and a second, more pronounced set, that originated at the outer edge of ceramic disk. The first set of radial cracks is in excellent agreement with the stress analysis based on using uniformly pressurized thick-walled cylinders. The set of radial cracks originating from the outer edge was unanticipated based on current damage models.

The measured radius of the comminuted/intact ceramic interface appears to coincide with the comminuted/intact ceramic interface radius that results in the maximum total strain energy within the intact section of the disk. Additional study and analysis will be required to verify any actual relationship.

The strain energy density from the internal pressurization of the ceramic disk/cylinder resulting from the penetration process is insufficient to initiate cracking at the outer edge of the ceramic disk. The most likely cause of this second set of radial cracks is the reflection of the shock wave from a ceramic-steel or ceramic-adhesive interface. Current damage models will have to be modified to account for the possibility of radial cracking initiating from the outer ceramic boundaries.
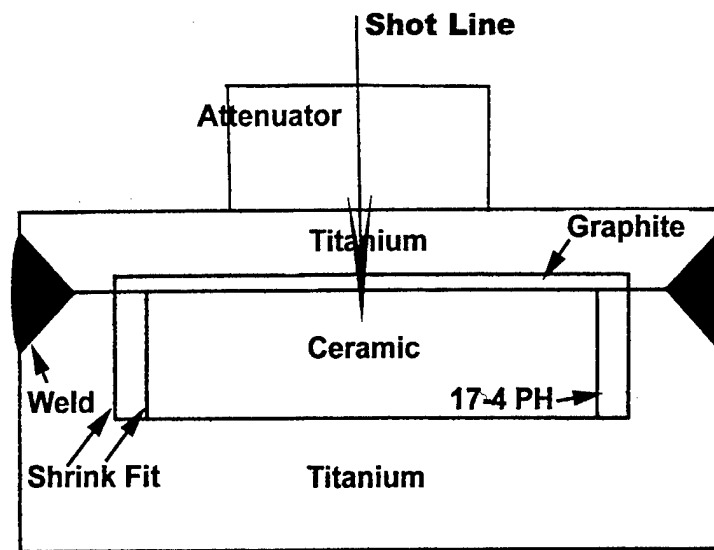
Figure 1. General target description.
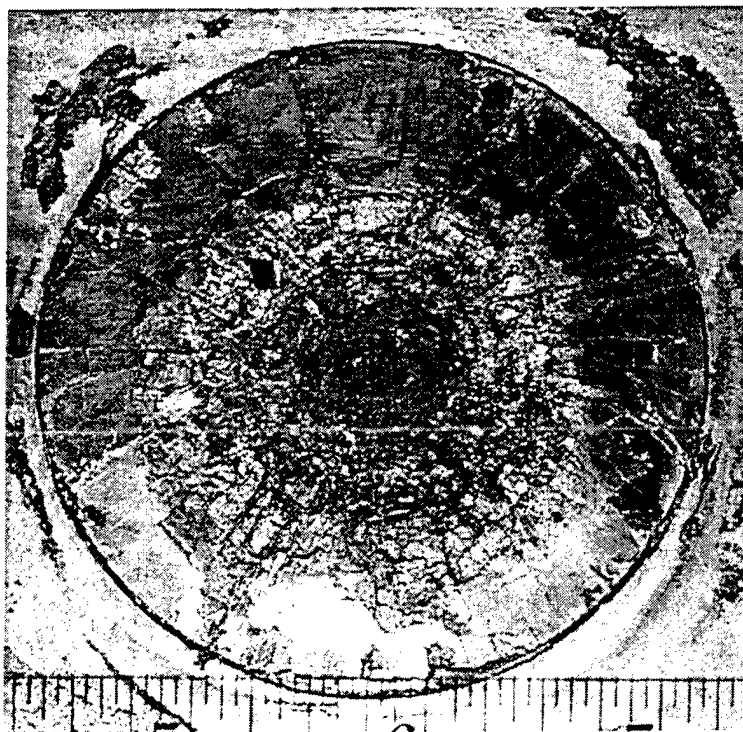
Figure 2. TiB$_2$ disk without prestress; single impact.

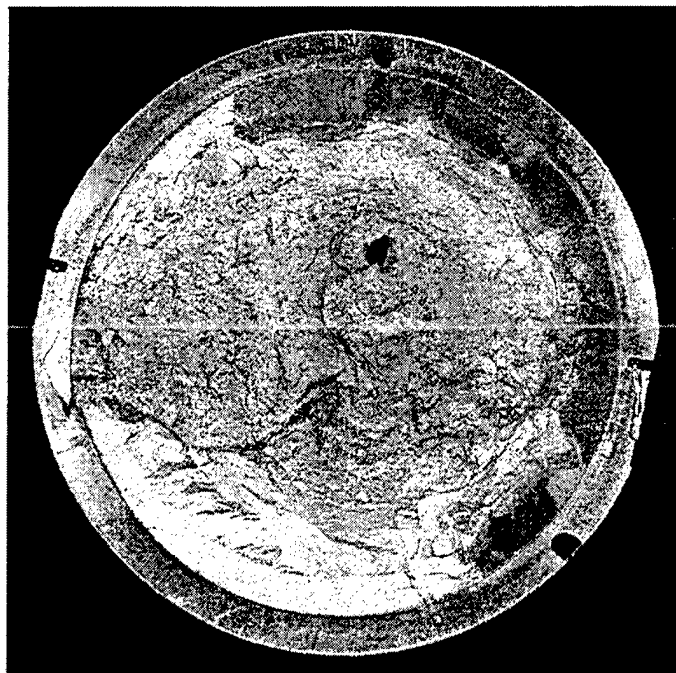Figure 3. TiB$_2$ disk with prestress; single impact.

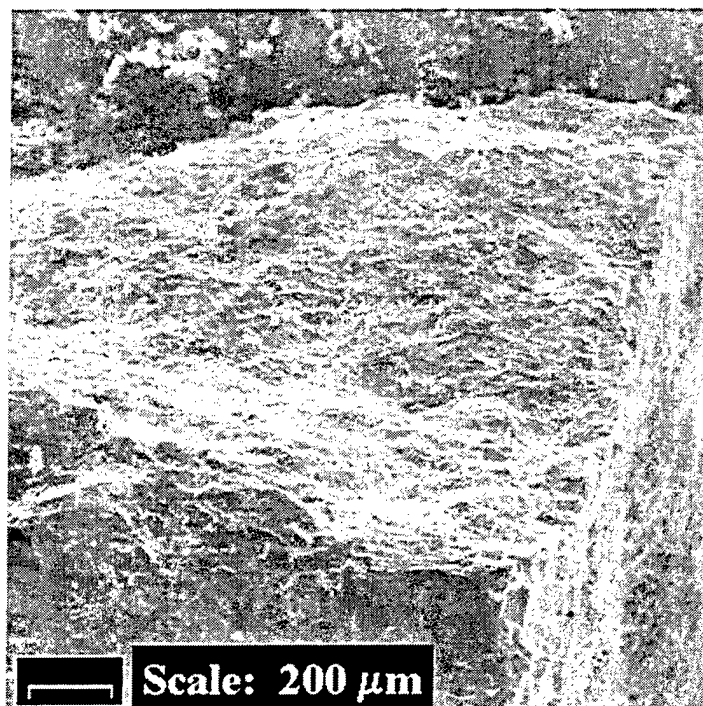Figure 4. TiB$_2$ with prestress; dual impact—front surface.

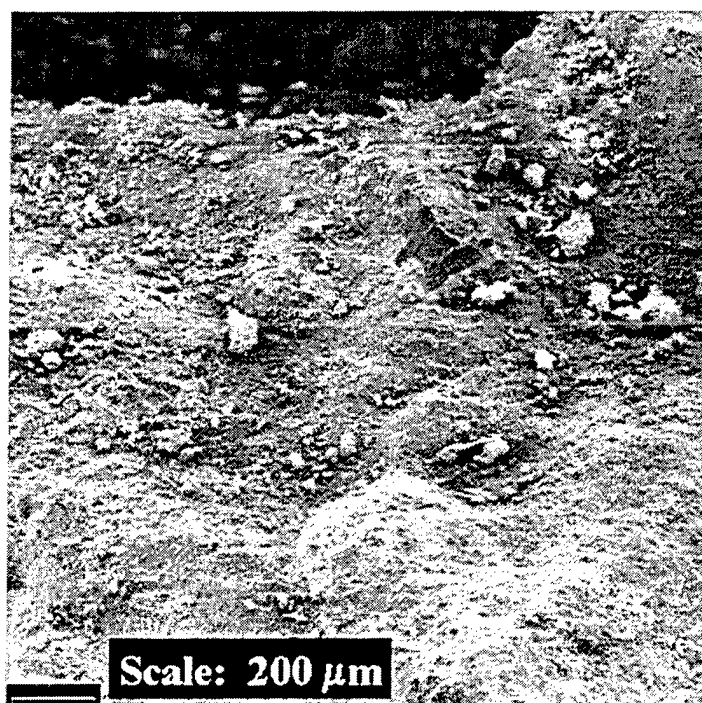Figure 5. SEM image of single impacted disk.
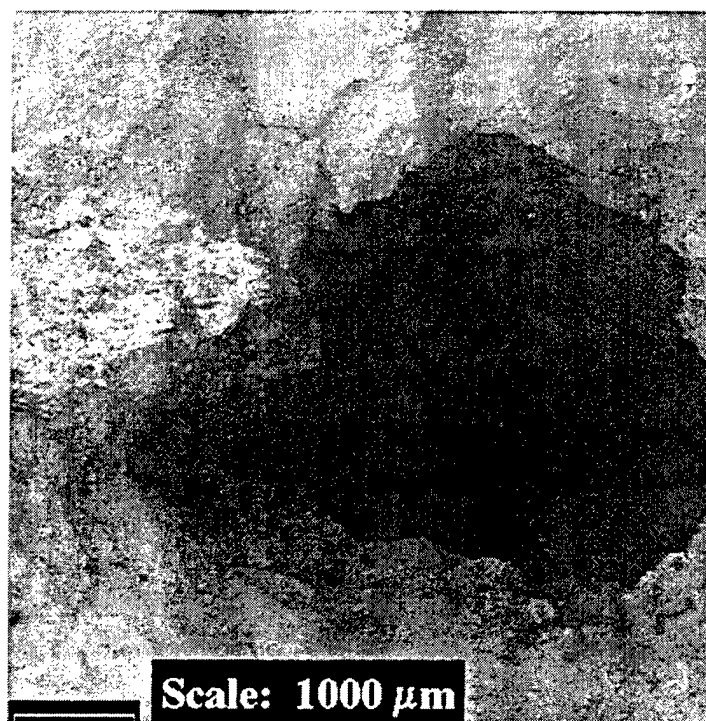

Figure 6. SEM image of dual impacted disk.

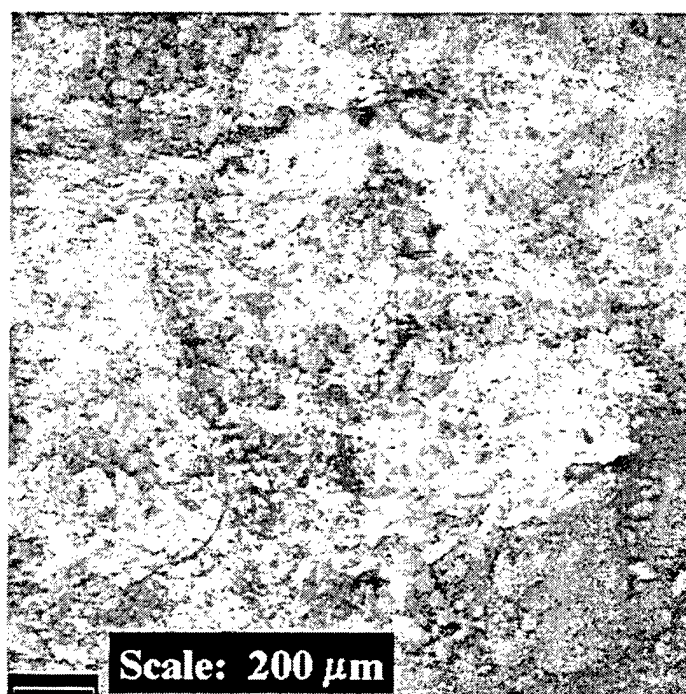Figure 7. SEM image in area of crater from second impact on disk.

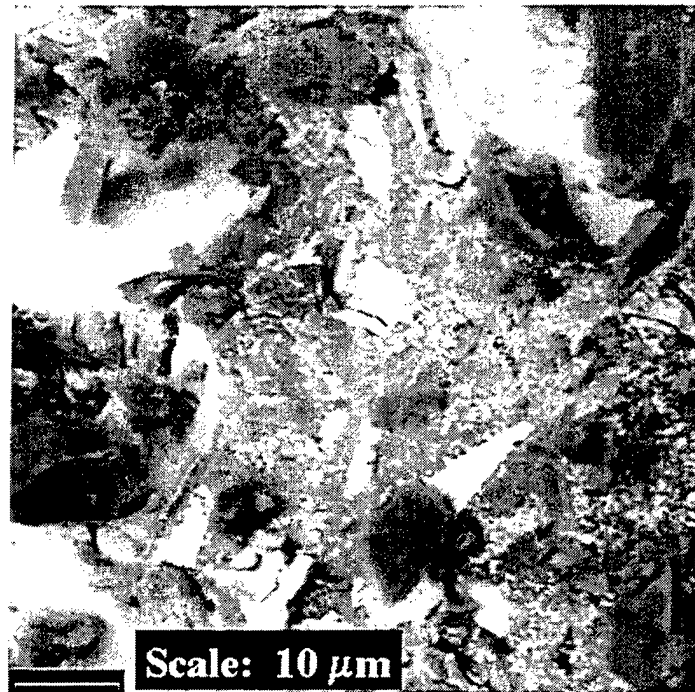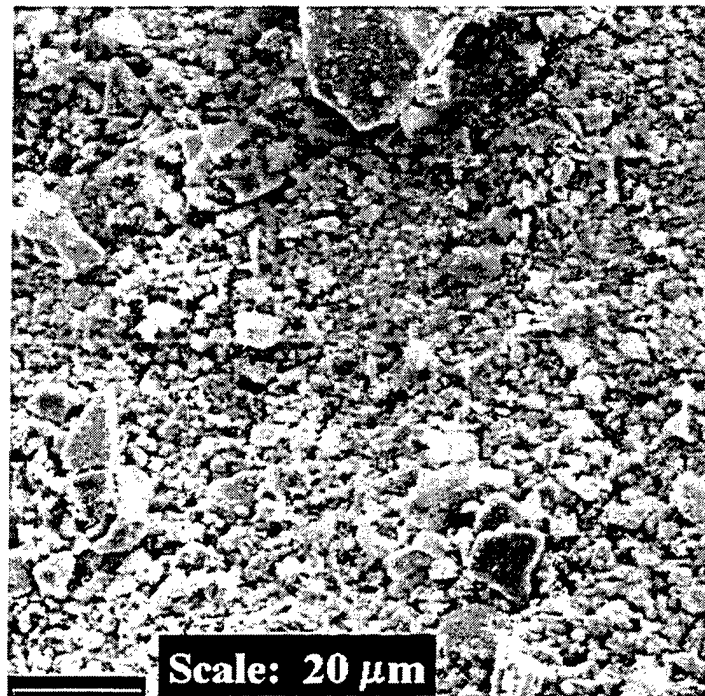Figure 8. SEM image of tungsten region near penetration channel.

19

Figure 9. Higher magnification image of tungsten region.

Figure 10. SEM image 3 mm from penetration channel.
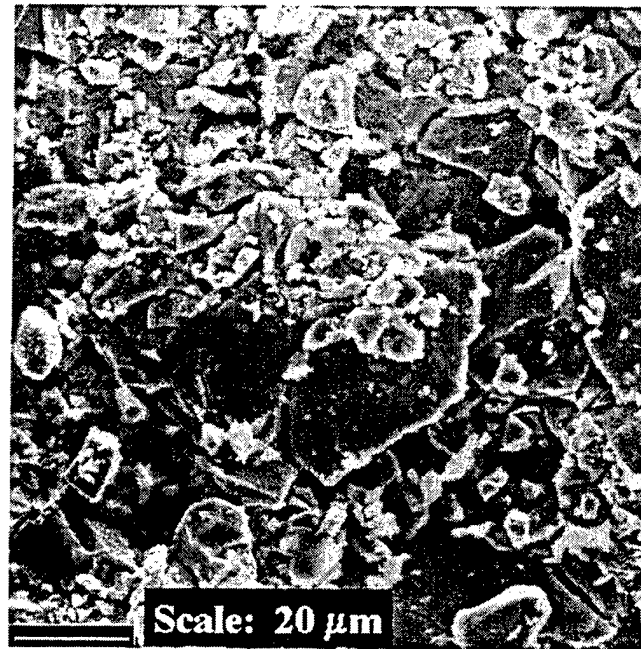
Figure 11. SEM image 13 mm from penetration channel.
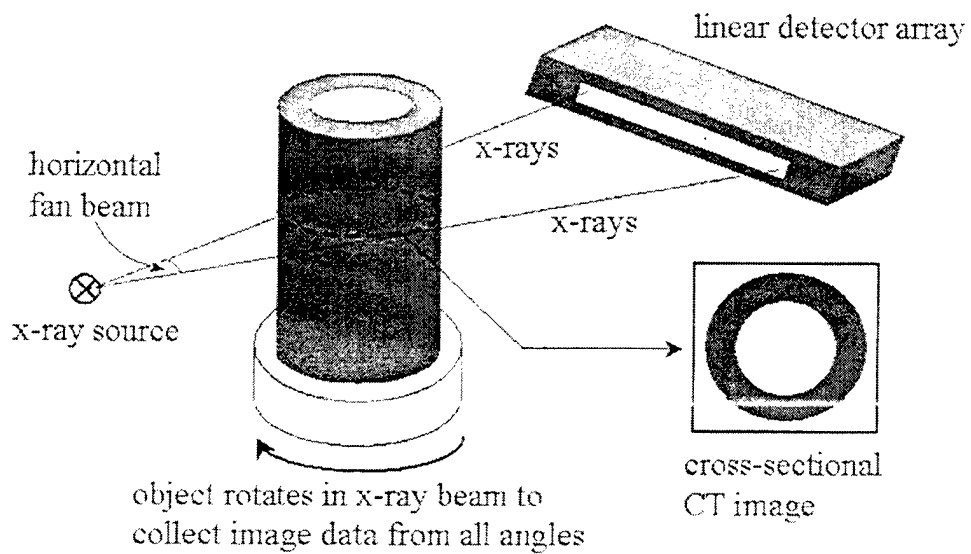
Figure 12. Schematic of RO CT scan technique.
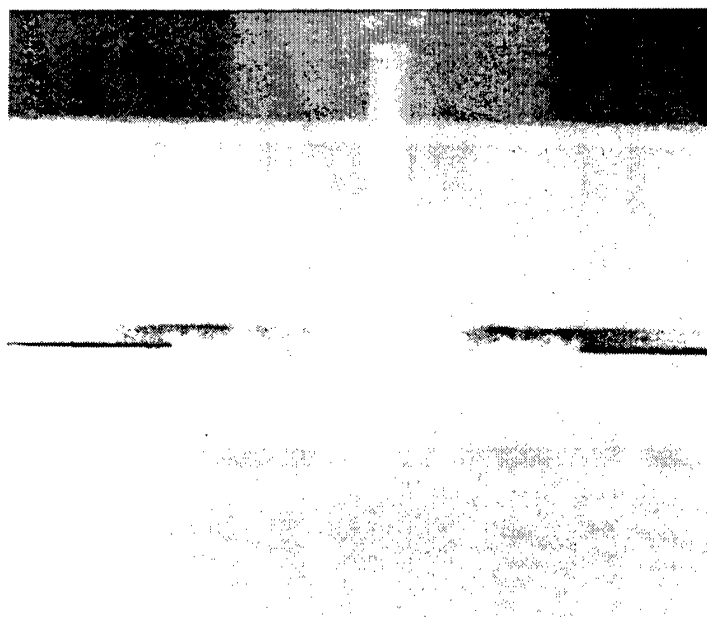
Figure 13. Flash radiograph of penetrating rod during test no. R-7.
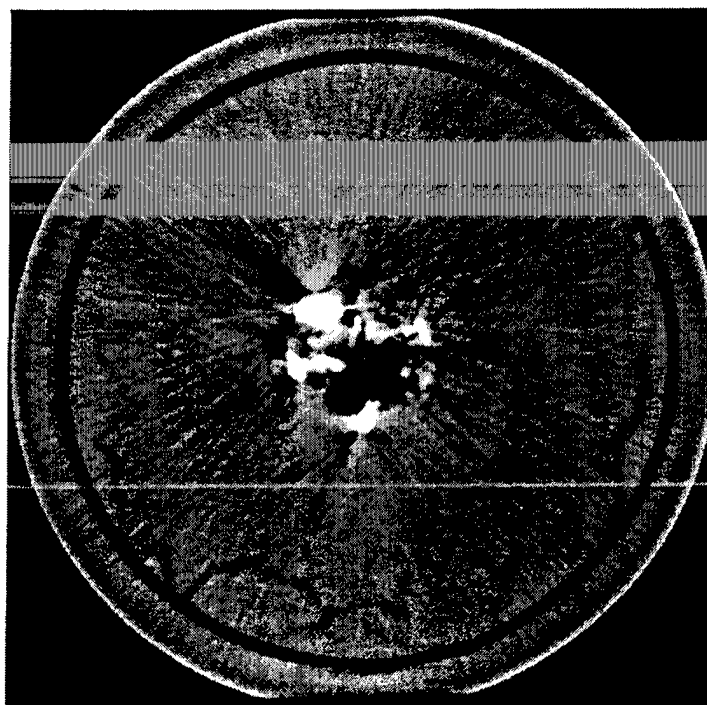
Figure 14. CT slice 21.0 mm from impact face of TiB_2 disk in test no. R-7.
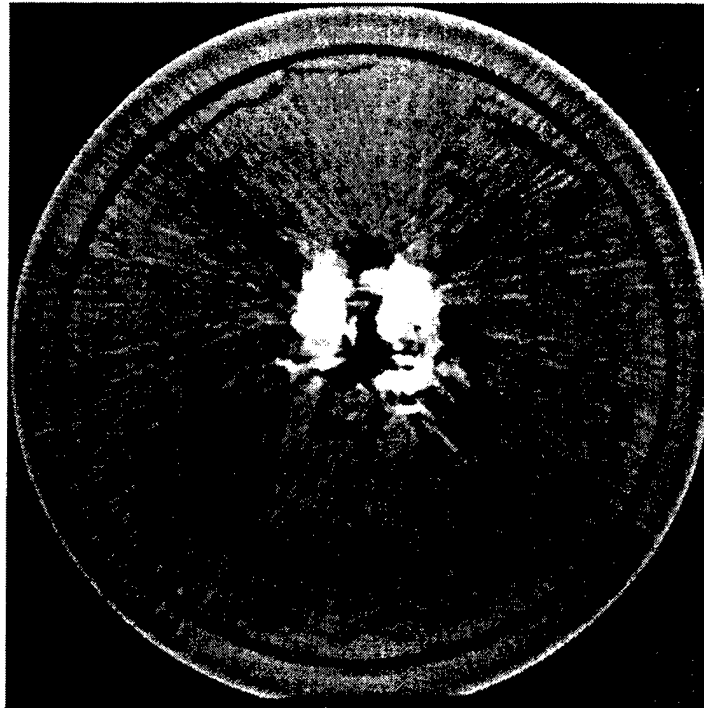
Figure 15. CT slice 4.5 mm from impact face of TiB$_2$ disk from test no. R-7.
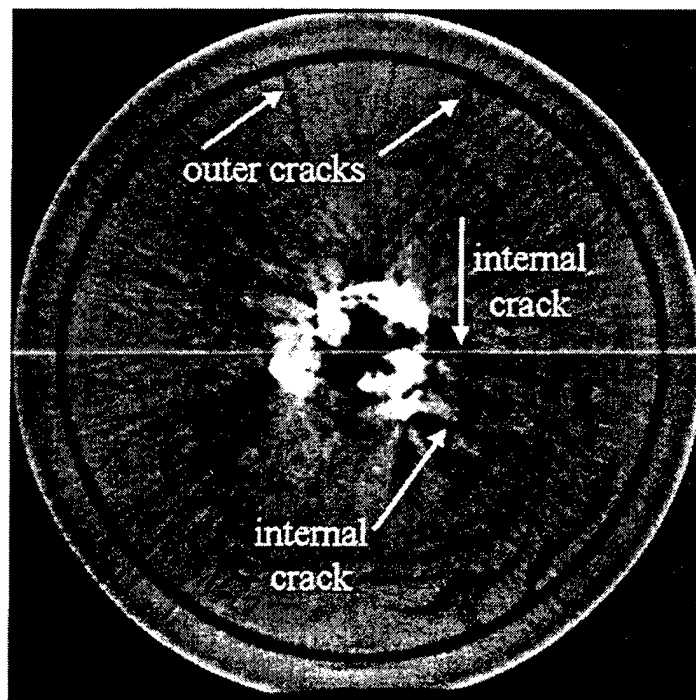
Figure 16. CT slice 3.0 mm from impact face showing two outer radial cracks in the TiB$_2$ disk from test no. R-7.
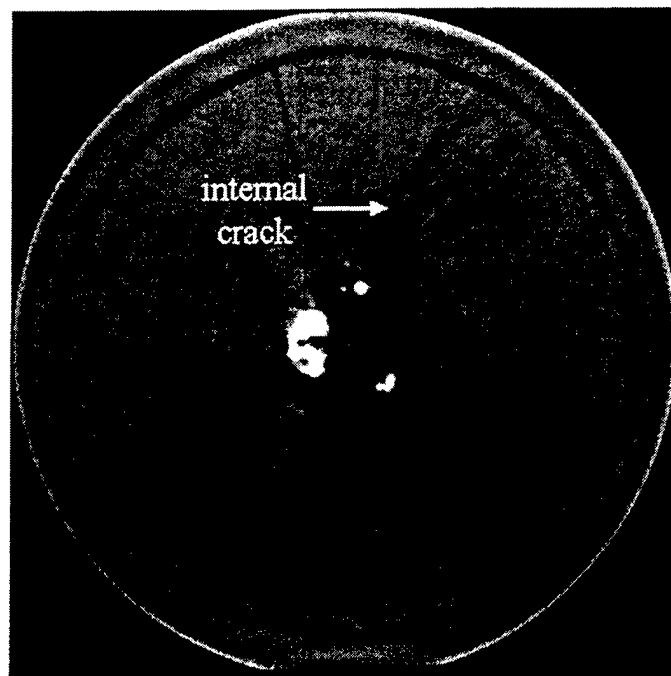
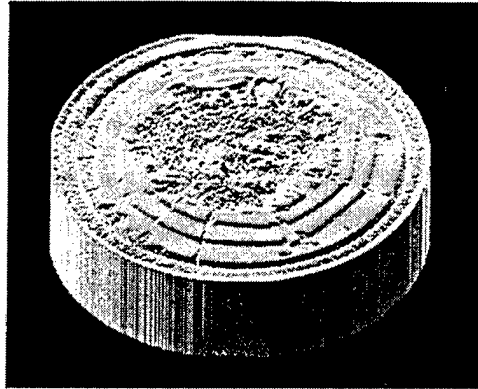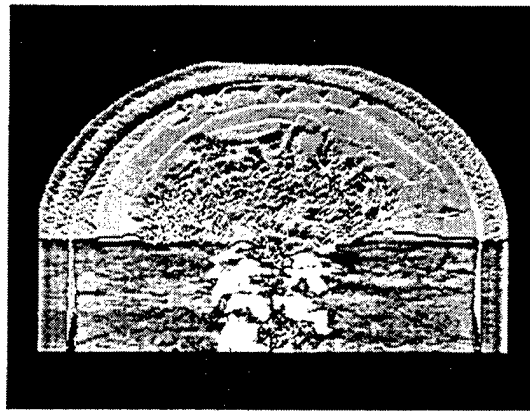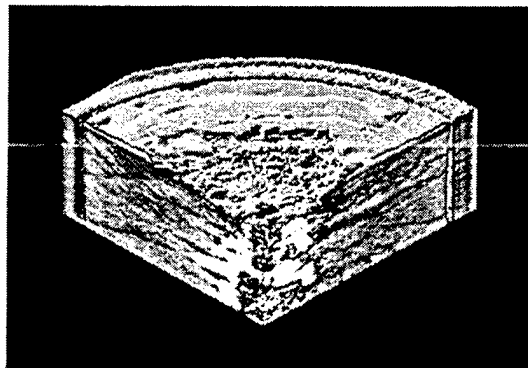Figure 17. CT slice 1.0 mm from impact face of TiB_2 disk from test no. R-7.
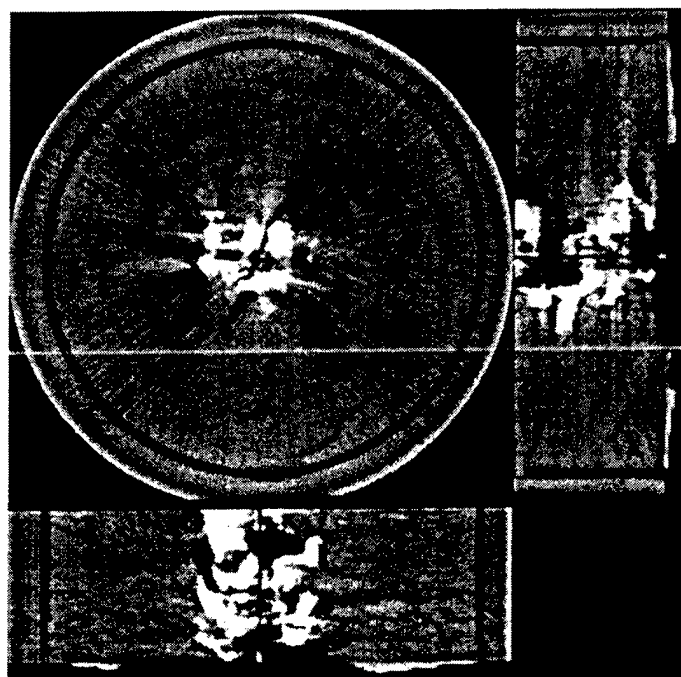
Figure 18. MPR image showing three perpendicular slice views for the TiB_2 disk from test no. R-7.

(a) 3-D solid image of the entire disk with the impact face at the top of the image.
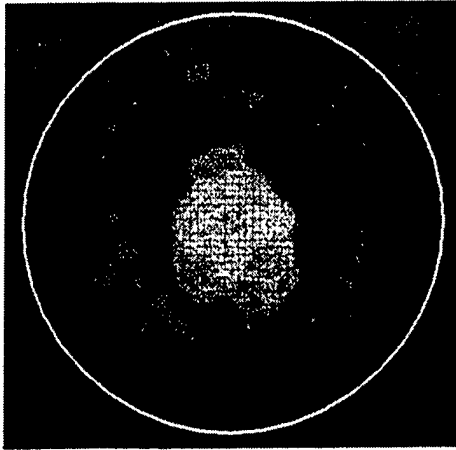

(b) 3-D solid image of the disk with approximately half of it "virtually" cut off perpendicular to the impact face.
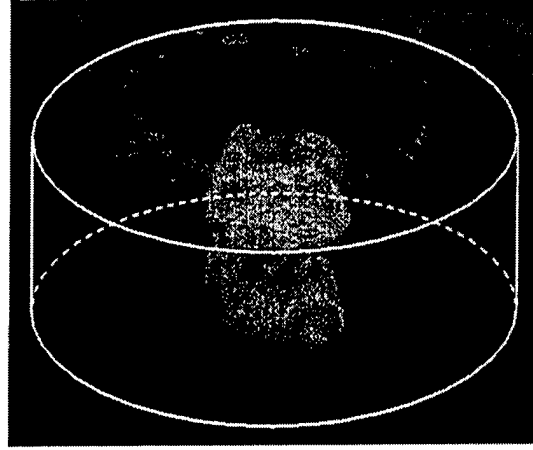

(c) 3-D solid image showing only 1/4 of the entire disk.

Figure 19. 3-D solid images of the TiB$_2$ disk from test no. R-7.

(a)   (b)

Figure 20. Penetrator point cloud (a) through-thickness view, and (b) oblique impact surface view from the TiB_2 disk used in test no. R-7.
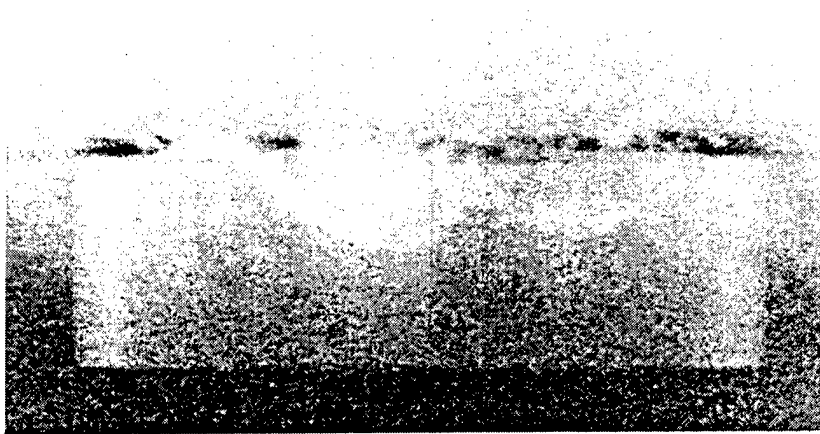

Figure 21. Test no. R-7 post-mortem radiograph of residual penetrator material (first impact).
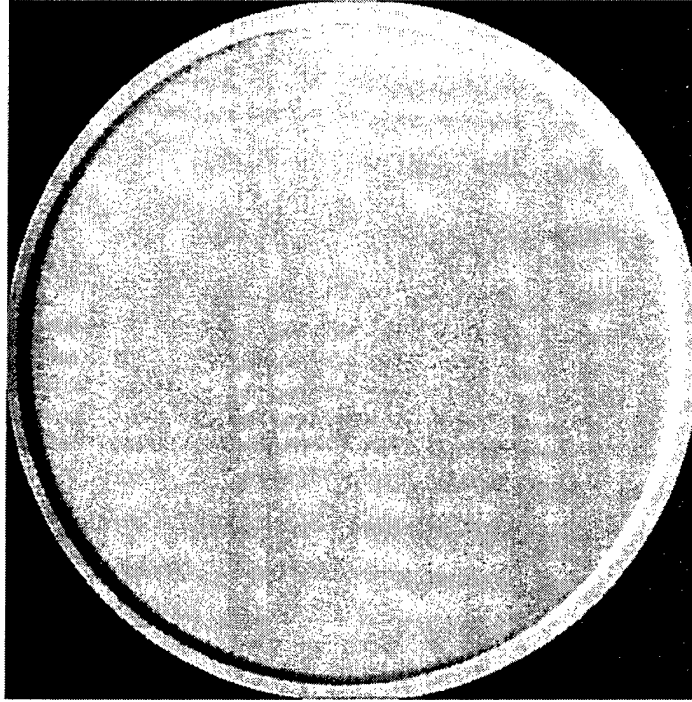
Figure 22. CT slice 22.5 mm from impact face of the TiB$_2$ disk used in test no. 340.
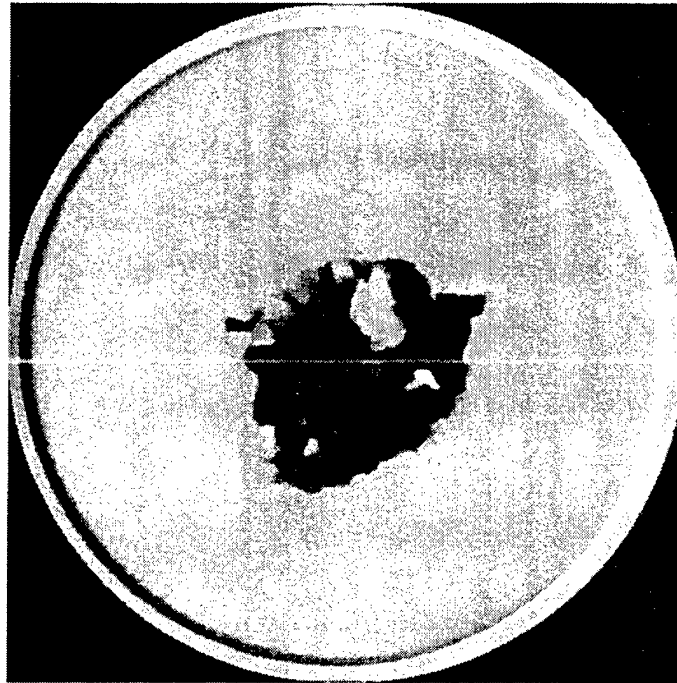

Figure 23. CT slice 3.0 mm from impact face of the TiB$_2$ disk used in test no. 340.

Figure 24. R-1 (2nd) post-mortem radiograph of combined residual penetrator material (after second impact).

Figure 25. CT slice 23.5 mm from impact face of the TiB$_2$ disk used in test no. R-1 (2nd).
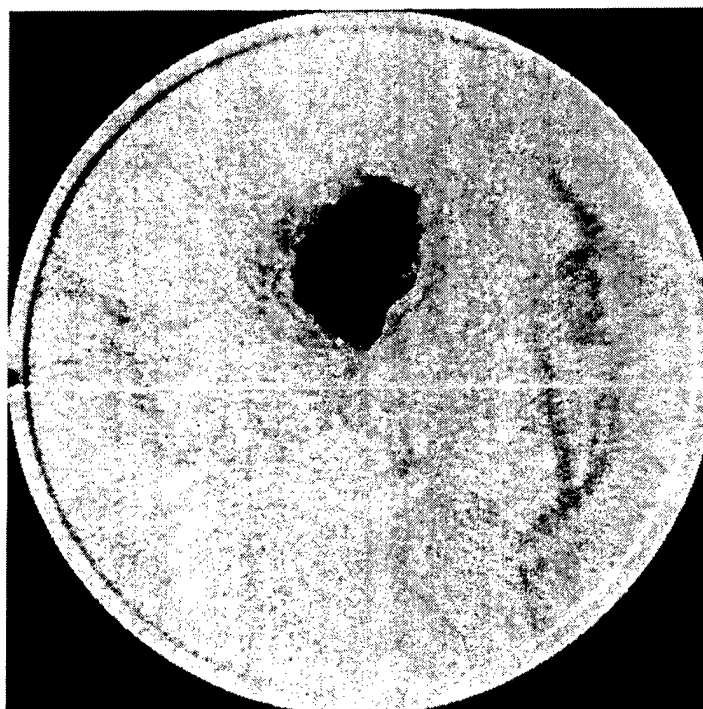
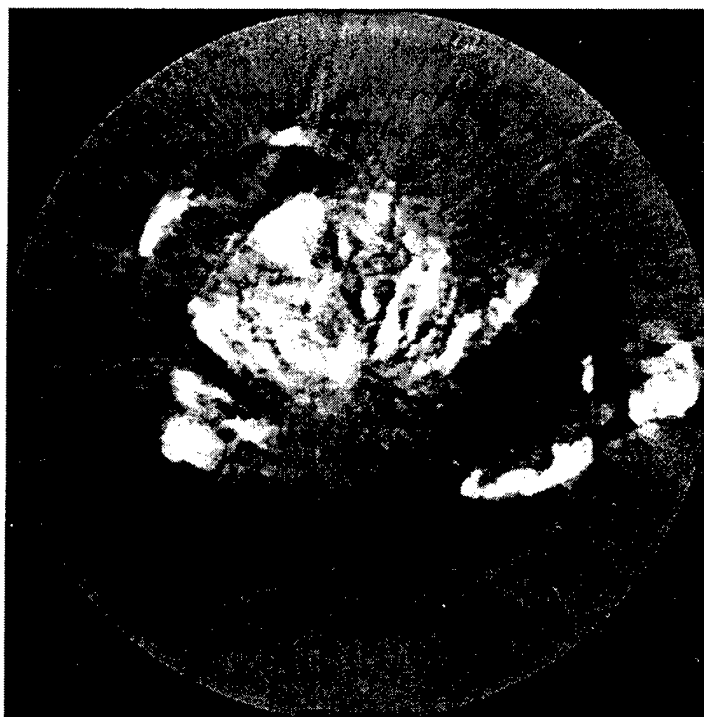Figure 26. CT slice 3.5 mm from impact face of the TiB$_2$ disk used in test no. R-1 (2nd).
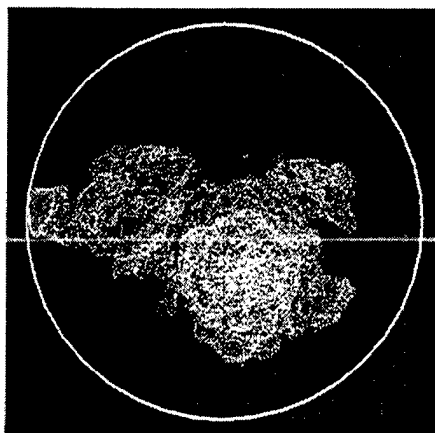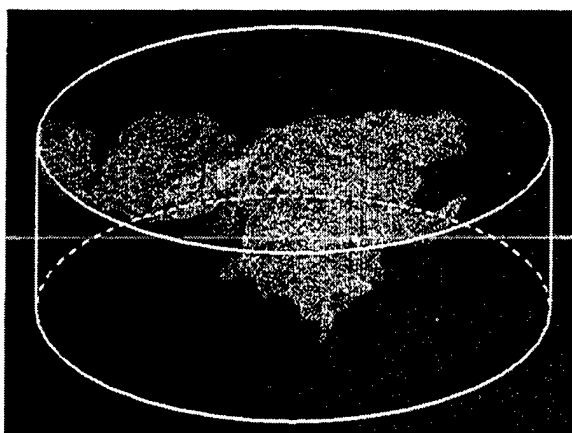
(a)   (b)

Figure 27.   Combined residual penetrator point cloud of the TiB$_2$ disk used in
test no. R-1 (2nd).
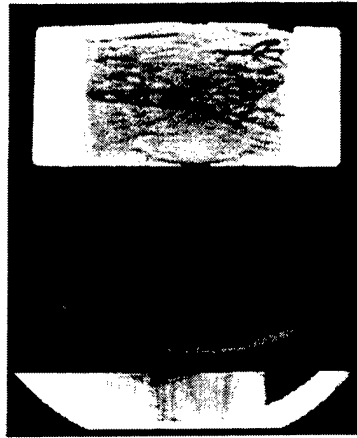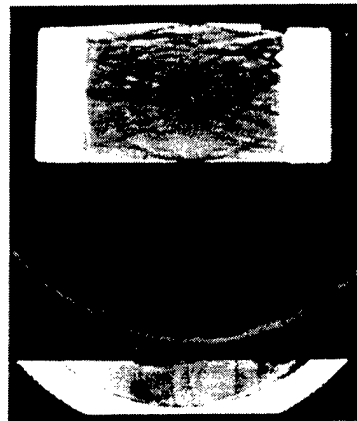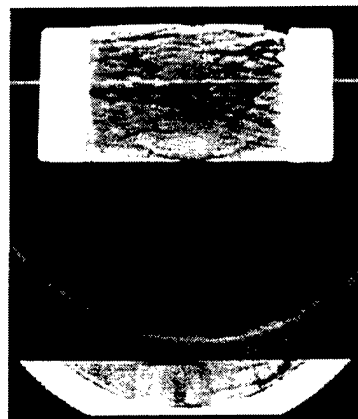
Figure 28. MPR images with FS (a) 0.97 mm, (b) 2.15 mm, and (c) 3.32 mm from impact face of the TiB$_2$ disk from test no. R-1 (2nd).
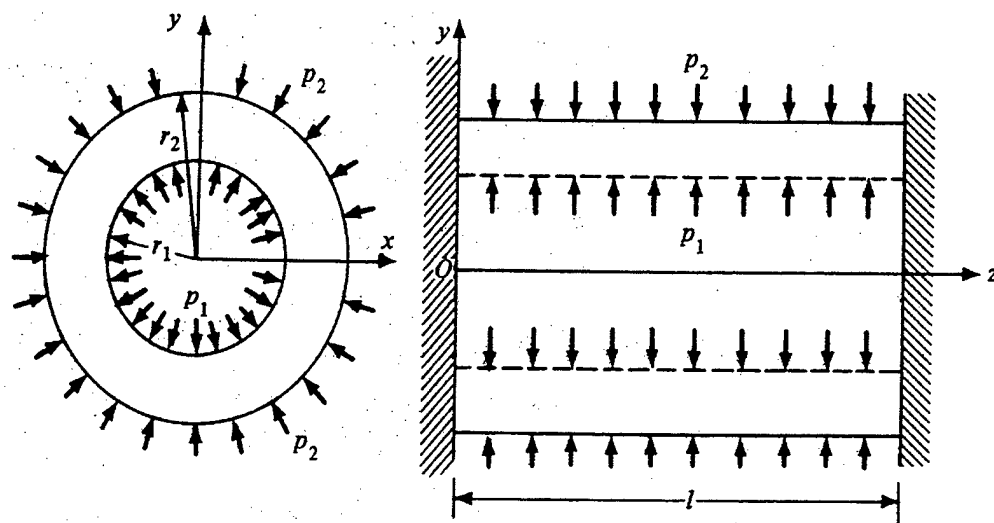
Figure 29. Generic pressure diagram.
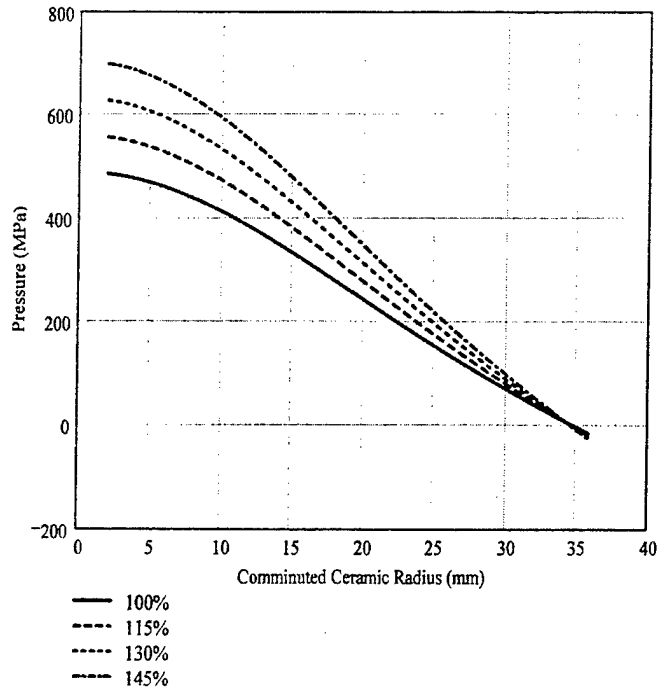
Figure 30. Internal pressures corresponding to percent hoop stress required to initiate fracture as function of comminuted ceramic radius.
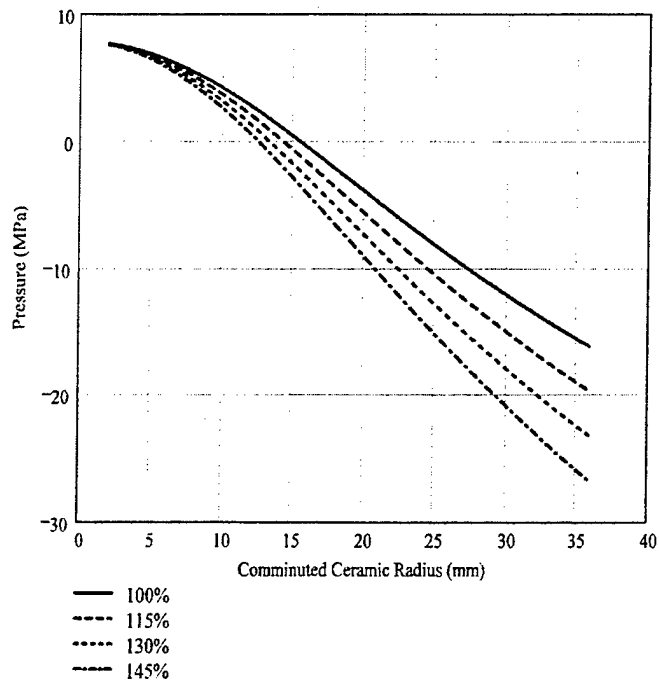
Figure 31. Pressures at ceramic/steel interface corresponding to percent hoop stress presented in Figure 30 as function of comminuted ceramic radius.
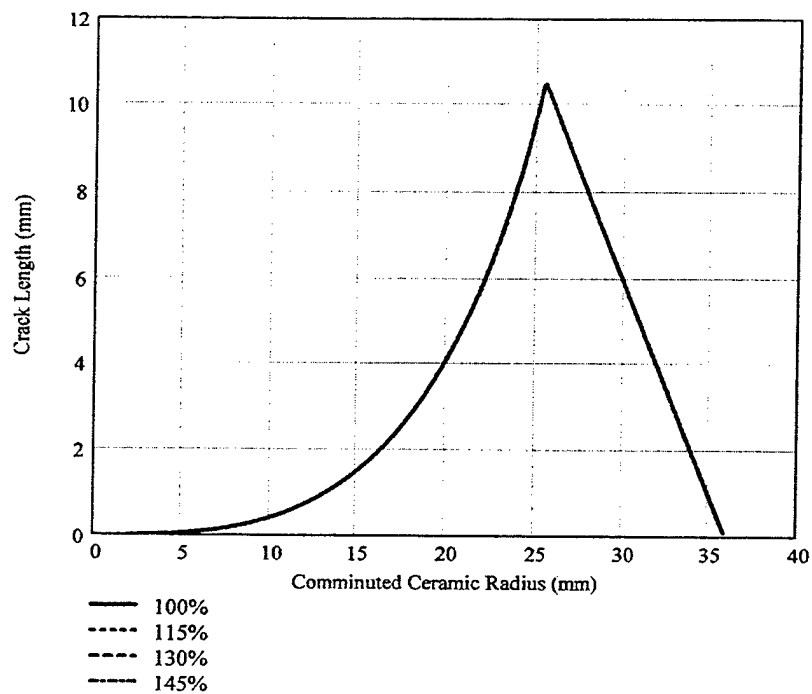
Figure 32. Maximum crack length between comminuted ceramic boundary and hoop stress tensile/compressive transition (or disk edge).
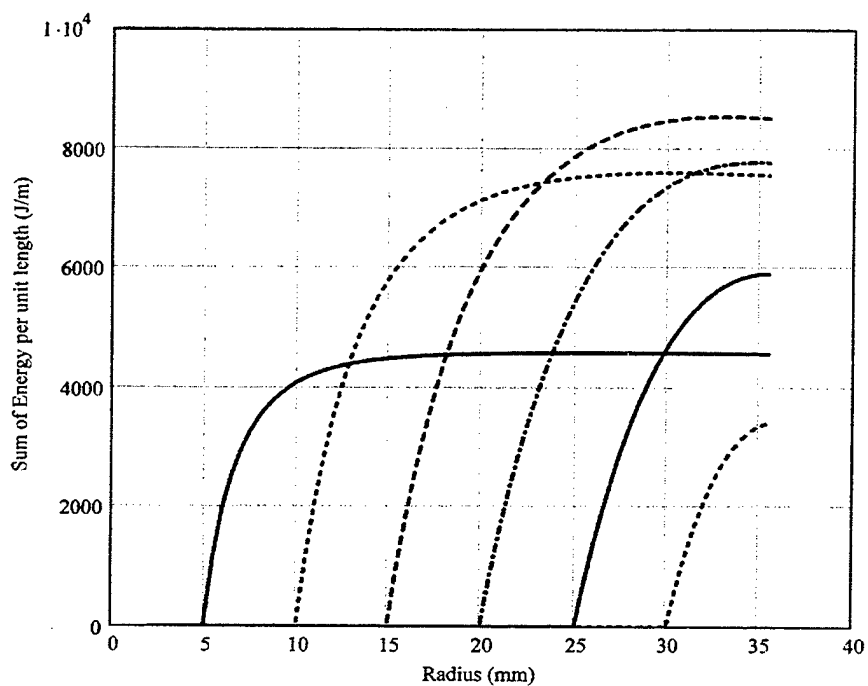
Figure 33. Sum of strain energy per unit length along the Z-axis for six comminuted/intact ceramic interface radii.

33

INTENTIONALLY LEFT BLANK.

6. References

Dennis, M. J. "Industrial Computed Tomography, American Society for Metals (ASM) International, ASM Handbook." *Nondestructive Evaluation and Quality Control*, vol. 17, pp. 358–386, 1989.

Dowding, R. J. U.S. Army Research Laboratory, Aberdeen Proving Ground, MD. 1999.

Grace, F. I. "Elastic Response and Potential Damage Zones in Ceramic Target Materials for Interface Defeat Under Rod Impact Conditions." Presented at International Ceramic Working Group Meeting (DOD/DOE), Aberdeen Proving Ground, MD, 23–24 April 1997.

Green, W. H., K. J. Doherty, N. L. Rupert, and J. M. Wells. "Damage Assessment in TiB_2 Ceramic Armor Targets." Part I: X-ray CT and SEM Analyses, *Proceedings of MSMS 2001, 2nd International Conference on Mechanics of Structures, Materials and Systems*, pp. 130–136, University of Wollongong, Wollongong, New South Wales, Australia, 14–16 February 2001.

Hauver, G. E., P. H. Netherwood, R. F. Benck, and L. J. Kecskes. "Ballistic Performance of Ceramic Targets." Proceedings of the Army Symposium on Solid Mechanics, Plymouth, MA, 17–19 August 1993.

Hauver, G. E., P. H. Netherwood, R. F. Benck, and L. J. Kecskes. "Enhanced Ballistic Performance of Ceramics." 19th Army Science Conference, Orlando, FL, 20–24 June 1994.

Hauver, G. E., P. H. Netherwood, R. F. Benck, and E. J. Rapacki. "Interface Defeat of Long Rod Projectiles by Ceramic Armor." U.S. Army Research Laboratory, Aberdeen Proving Ground, MD, to be published.

Irwin, G. R., J. A. Keis, and H. L. Smith. "Fracture Strengths Relative to Onset and Arrest of Crack Propagation." *Proceedings of the American Society for Testing and Materials*, vol. 58, pp. 640–660, 1958.

Lamé, G. *Leçons sur la théorie mathématique de l'élasticité des corps solides*. Paris: Bachelier, 1852.

Lundberg, P., R. Renström, and B. Lundberg. "Impact of Metallic Projectiles on Ceramic Targets: Transition Between Interface Defeat and Penetration." *International Journal of Impact Engineering*, vol. 24, pp. 259–275, 2000.

Rupert, N. L., W. H. Green, K. J. Doherty, and J. M. Wells. "Damage Assessment in TiB$_2$ Ceramic Armor Targets: Part II - Radial Cracking," *Proceedings of MSMS 2001, 2nd International Conference on Mechanics of Structures, Materials and Systems,* pp. 137–144, University of Wollongong, Wollongong, New South Wales, Australia, 14–16 February 2001.

Stanley, J. H. "Physical and Mathematical Basis of CT Imaging, for American Society for Testing and Materials (ASTM)." ASTM CT Standardization Committee E7.01.07, ASTM Tutorial, section 3, Columbus, OH, 1985.

Teledyne Firth Sterling. Material certification sheet. U.S. Army Ballistic Research Laboratory contract number DAAD05-90-C-0431, LaVergne, TN, 1991.

Trevino, S., G. Hauver, E. Rapacki, J. Wells, and P. Brand. "Stress Measurements in SiC Target Using Neutron Diffraction." Proceedings of the 21st Army Science Conference, Norfolk, VA, 15–17 June 1998.

Volterra, E., and J. H. Gains. *Advance Strength of Materials.* Englewood Cliffs, NJ: Prentice-Hall, Inc., 1971.

Wells, J. M., W. H. Green, and N. L. Rupert. "Nondestructive 3D Visualization of Ballistic Impact Damage in a TiC Ceramic Target Material." *Proceedings of MSMS 2001, 2nd International Conference on Mechanics of Structures, Materials and Systems,* pp. 159–166, University of Wollongong, Wollongong, New South Wales, Australia, 14–16 February 2001.

NO. OF COPIES	ORGANIZATION
2	DEFENSE TECHNICAL INFORMATION CENTER DTIC OCA 8725 JOHN J KINGMAN RD STE 0944 FT BELVOIR VA 22060-6218
1	HQDA DAMO FDT 400 ARMY PENTAGON WASHINGTON DC 20310-0460
1	OSD OUSD(A&T)/ODDR&E(R) DR R J TREW 3800 DEFENSE PENTAGON WASHINGTON DC 20301-3800
1	COMMANDING GENERAL US ARMY MATERIEL CMD AMCRDA TF 5001 EISENHOWER AVE ALEXANDRIA VA 22333-0001
1	INST FOR ADVNCD TCHNLGY THE UNIV OF TEXAS AT AUSTIN 3925 W BRAKER LN STE 400 AUSTIN TX 78759-5316
1	US MILITARY ACADEMY MATH SCI CTR EXCELLENCE MADN MATH THAYER HALL WEST POINT NY 10996-1786
1	DIRECTOR US ARMY RESEARCH LAB AMSRL D DR D SMITH 2800 POWDER MILL RD ADELPHI MD 20783-1197
1	DIRECTOR US ARMY RESEARCH LAB AMSRL CI AI R 2800 POWDER MILL RD ADELPHI MD 20783-1197

NO. OF COPIES	ORGANIZATION
3	DIRECTOR US ARMY RESEARCH LAB AMSRL CI LL 2800 POWDER MILL RD ADELPHI MD 20783-1197
3	DIRECTOR US ARMY RESEARCH LAB AMSRL CI IS T 2800 POWDER MILL RD ADELPHI MD 20783-1197

ABERDEEN PROVING GROUND

2	DIR USARL AMSRL CI LP (BLDG 305)

38

NO. OF COPIES	ORGANIZATION	NO. OF COPIES	ORGANIZATION
3	NAVAL RSCH LABORATORY B METZBOWER D MICHEL R KERANS 4555 OVERLOOK AVE SW WASHINGTON DC 20375	6	SANDIA NATL LAB R GRAHAM DIV 1551 P YARRINGTON D GRADY MS 0821 L CHHABILDAS MS 0821 TECH LIBRARY PO BOX 5800 ALBUQUERQUE NM 87185-0307
13	DIR LOS ALAMOS NATL LAB G E CORT F663 R KARPP MS 1960 F GAC B HOGAN W GASKILL J CHAPYAK MS G787 S MARSH MS 970 M 6 T N CLAYTON M H JONES R M BONITA D M WRIGHT K E SIMMONDS MS 6352 TECH LIBRARY PO BOX 1663 LOS ALAMOS NM 87545	1	CIA OSWR DSD W WALTMAN RM 5P0110 NHB WASHINGTON DC 20505
		1	FEDERAL HIGHWAY ADMINSTR G WASHER NONDEST VALIDATION CTR TURNER FAIRBANK HWY RES CTR 6300 GEORGETOWN PIKE MCLEAN VA 22101
2	AIR FORCE ARMAMENT LAB AFATL DLJW W COOK TECH LIBRARY EGLIN AFB FL 32542	7	INST FOR ADVNCD TECH W REINECKE S BLESS H FAIR P SULLIVAN T KIEHNE D LITTLEFIELD R SUBRAMANIAN PO BOX 202797 AUSTIN TX 78720-2797
2	MSD ENL W DYESS J FOSTER EGLIN AFB FL 32542-5000	2	UNIV OF DAYTON RSCH INST KLA14 N BRAR A PIEKUTOWSKI 300 COLLEGE PARK DAYTON OH 45469-0182
1	NEW MEXICO TECH D EMARY TERA GROUP SOCORRO NM 87801	3	SOUTHWEST RSCH INST C ANDERSON J RIEGEL J WALKER 6220 CULEBRA RD SAN ANTONIO TX 78238
1	DEFENSE NUCLEAR AGENCY TECH LIBRARY 6801 TELEGRAPH RD ALEXANDRIA VA 22192	2	BROWN UNIV DIV OF ENGINEERING R CLIFTON S SUNDARAM PROVIDENCE RI 02912

NO. OF COPIES	ORGANIZATION	NO. OF COPIES	ORGANIZATION
3	O GARA HESS AND EISENHARDT G ALLEN D MALONE T RUSSELL 9113 LE SAINT DR FAIRFIELD OH 45014	3	UNITED DEFENSE LP E BRADY R JENKINS J JOHNSON PO BOX 15512 YORK PA 17405-1512
1	OREMET WAH CHANG Y KOSAKA PO BOX 460 ALBANY OR 97321	1	ZERNOW TECH SVCS INC L ZERNOW 425 W BONITA AVE SUITE 208 SAN DIMAS CA 91773
4	POULTER LABORATORY SRI INTERNATIONAL D CURRAN R KLOOP L SEAMAN D SHOCKEY 333 RAVENSWOOD AVE MENLO PARK CA 94025	1	PNIN DPTY FOR TCHNLGY HQ US ARMY MATCOM AMCDCG T 5001 EISENHOWER AVE ALEXANDRIA VA 22333-0001
1	SAIC J FURLONG MS 264 1710 GOODRIDGE DR MCLEAN VA 22102	1	PNIN DPTY FOR ACQUSTN HQ US ARMY MATCOM AMCDCG A 5001 EISENHOWER AVE ALEXANDRIA VA 22333-0001
1	BOB SKAGGS RT 11 BOX 81E SANTA FE NM 87501	1	DPTY CG FOR RDE HQS US ARMY MATCOM AMCRD 5001 EISENHOWER AVE ALEXANDRIA VA 22333-0001
4	SIMULA INC R WOLFFE R HUYETT G GRACE G YANIU 10016 SOUTH 51ST ST PHOENIX AZ 85044	1	DPTY ASSIST SCY FOR R&T SARD TT THE PENTAGON WASHINGTON DC 20301-7100
8	UNITED DEFENSE LP J DORSCH V HORVATICH B KARIYA M MIDDIONE J MORROW R MUSANTE R RAJAGOPAL D SCHADE PO BOX 367 SANTA CLARA CA 95103	1	OSD OUSD(A&T)/ODDR&E (W) L SLOTER 1777 N KENT ST SUITE 9030 ARLINGTON VA 22209
		1	US MILITARY ACADEMY DEPARTMENT OF MATH SCI WEST POINT NY 10996-1786
		2	DIR DARPA S WAX L CHRISTODOULOU 3701 NORTH FAIRFAX DR ARLINGTON VA 22203-1714

NO. OF COPIES	ORGANIZATION	NO. OF COPIES	ORGANIZATION
2	CDR USAF RSCH LAB W GRIFFITH J MALAS WPAFB OH 45433-7131	1	DIRECTOR NTIAC G A MATZKANIN 415 CRYSTAL CREEK DR AUSTIN TX 78746
2	UNIV OF CA SAN DIEGO DEPT OF EXPERIMENTAL MECH AND STRUCTURAL ENGR V M KARBHARI F L DISCALEA LA JOLLA CA 92093-0085	2	MATERIEL TEST DIR CSTE DTC WS MT H W BENNETT R GRAJEDA WSMR NM 88002
2	THE JOHNS HOPKINS UNIV R E GREEN J B SPICER 102 MARYLAND HALL 3400 N CHARLES ST BALTIMORE MD 21218	2	CDR US ARMY MRDEC AMSMI RD ST WF D LOVELACE M SCHEXNAYER REDSTONE ARSENAL AL 34898-5250
5	PENN STATE UNIV DEPT SCI & MECH R MCNITT B TITTMANN C LIFFENDEN DEPT CIVIL ENG R QUEENEY T KRAUTHAMMER ENRGY & GEO ENVIR ENG A S GRADER UNIVERSITY PARK PA 16802	2	CDR US ARMY ARDEC SMCAR AAE W J PEARSON TECH LIBRARY PICATINNY ARSENAL NJ 07806-5000
2	NSWC INDIAN HD DIV CONCORD DETACHMENT CODE 722 M SKIPALIS W BROWN 10 DELTA ST CONCORD CA 94520-5100	1	PM TANK MAIN ARMNT SYS SSAE AR TMA MT PICATINNY ARSENAL NJ 07806-5000
1	NASA LANGLEY RSCH CNTR NDE SCI BRANCH J N ZALAMEDA BLDG 1230 RM 154 HAMPTON VA 23681-0001	2	CDR ERO USARDSG (UK) S SAMPATH J ILLINGER PSC 802 BOX 15 FPO AE 09499-1500
1	DIRECTOR AMPTIAC D ROSE 201 MILL ST ROME NY 13440-6916	1	CHIEF OF NAVAL RSCH OFC OF NAVAL TECH A J FAULSDITCH ONT 23 BALLSTON TOWERS ARLINGTON VA 22217
		1	NAVAL WPNS CTR TECH LIBRARY CHINA LAKE CA 93555
		1	NUSC NEWPORT S DICKINSON CODE 8214 NEWPORT RI 02841

NO. OF COPIES	ORGANIZATION	NO. OF COPIES	ORGANIZATION
1	NAWC J J LUNDEEN CODE 4342 BLDG 2188 PATUXENT RIVER MD 20670-1908	1	DOW CHEMICAL INC K EPSTEIN ORDNANCE SYS 800 BUILDING MIDLAND MI 48667
14	NSWC DAHLGREN DIV V GEHMAN B20 E E ROWE G22 (5 CPS) B D SMITH G22 (5 CPS) J MCCONKIE G32 TECH LIBRARY B60 MISSILE SYS DATA CTR G205B 17320 DAHLGREN RD DAHLGREN VA 22448	1	CALKINS R&D INC N CALKINS 515 SEWARD PK AVE ALBUQUERQUE NM 87123
		1	CORNING INC S HAGG SP DV 22 CORNING NY 14831
3	DYNA EAST CORP P C CHOU R CICCARELLI W FLIS 3610 HORIZON DR KING OF PRUSSIA PA 19406	1	UNIV OF DAYTON R HOFFMAN 300 COLLEGE PARK DAYTON OH 45469
2	S CUBED R SEDGWICK PO BOX 1620 LA JOLLA CA 92038-1620	1	ROCKWELL INTL ROCKETDYNE DIV J MOLDENHAUER 6633 CANOGA AVE HB 23 CANOGA PK CA 91303
1	LIVERMORE SOFTWARE TECH CORP J O HALLQUIST 1876 WAVERLY WAY LIVERMORE CA 94550	2	ALLIED SIGNAL L LIN PO BOX 31 PETERSBURG VA 23804
1	SCHWARZKOPFF TECH CORP E KOSINISKI 35 JEFFREY AVE HOLLISTON MA 01746	1	MCDONNELL DOUGLAS HELICOPTER L R BIRD MS 543 D216 5000 E MCDOWELL RD MESA AZ 85205
1	PRIMEX CORP D EDMONDS 10101 9TH ST N ST PETERSBURG FL 33716	1	BOEING CORP T M MURRAY MS 84 84 PO BOX 3999 SEATTLE WA 98124
1	BATTELLE D TROTT 505 KING AVE COLUMBUS OH 43201	1	EMBASSY OF AUSTRALIA COUNSELLOR DEFENCE SCIENCE 1601 MASSACHUSETTS AVE NW WASHINGTON DC 20036-2273
1	RAYTHEON CO R LLOYD PO BOX 1201 TEWKSBURY MA 01876		

NO. OF COPIES	ORGANIZATION
1	MILITARY VEHICLES AND ORDNANCE REPORT L S NESS 20 EAST DEL RAY AVE ALEXANDRIA VA 22301
1	TRACOR AEROSPACE R E BROWN PO BOX 196 SAN RAMON CA 94583
1	AEROJET J CARLEONE PO BOX 13222 SACRAMENTO CA 95813-6000
1	NDIA L F SKIBBIE 2101 WILSON BLVD STE 400 ARLINGTON VA 22201-3061
2	UNIV OF TEXAS AT EL PASO MATERIALS ENGINEERING L E MURR MAIL CODE 00520 EL PASO TX 79968
1	F I GRACE 90 CHURCHILL DR YORK PA 17403
8	J J FROST S REYNOLDS ST APT 1001 ALEXANDRIA VA 22304
1	H T YOLKEN TRI AUSTIN 15400 EDWARDS FERRY RD POOLESVILLE MD 20837
1	GENERAL ELECTRIC COMPANY CORPORATE R & D C BUENO BLDG KW RM D246 PO BOX 8 SCHENECTADY NY 12301-0008
1	INDUSTRIAL QUALITY INC T S JONES VP 640 EAST DIAMOND AVE SUITE C GAITHERSBURG MD 20877-5323

NO. OF COPIES	ORGANIZATION
2	WISS JANNEY ELSTNER ASSOC H H SALEH R LIVINGSTON NONDEST VALIDATION CTR TURNER FAIRBANK HWY RES CTR 6300 GEORGETOWN PIKE MCLEAN VA 22101
2	MSE INC HIGH PERFORMANCE MAT GRP K LEIGHTON 1300 MARROWS ROAD NEWARK DE 19711

ABERDEEN PROVING GROUND

NO. OF COPIES	ORGANIZATION
1	DIR USA EBCC SCBRD RT 5183 BLACKHAWK RD APG MD 21010-5424
1	CDR USA SBCCOM AMSCB CII 5183 BLACKHAWK RD APG MD 21010-5424
2	DIR USAMSAA AMXSY D AMXSY MP H COHEN BLDG 392 APG MD 21005
1	CDR USATEC AMSTE TC RYAN BLDG APG MD 21005
3	CDR USAATC STEAC LI LV E SANDERSON M SIMON (2 CPS) BLDG 400 APG MD 21005

44

ABERDEEN PROVING GROUND (CONT'D)

ABERDEEN PROVING GROUND (CONT'D)

97   DIR USARL
       AMSRL SL I
       AMSRL WM
         J SMITH
         M PETERSON
         E SCHMIDT
       AMSRL WM M
         D VIECHNICKI
         G HAGNAUER
         J MCCAULEY
       AMSRL WM MA
         S KNIGHT
       AMSRL WM MB
         B FINK
         T BOGETTI
         D GRANVILLE
         C HOPPEL
         P DEHMER
       AMSRL WM MC
         J BEATTY
         J WELLS (5 CPS)
         J ADAMS
         E CHIN
         G GILDE
         L LASALVIA
         J MONTGOMERY
         P PATEL
         A WERESZCZAK
       AMSRL WM MD
         W ROY
         W GREEN (5 CPS)
         P SINCEBAUGH
         S WALSH
         W DEROSSET
         R DOWDING
         V CHAMPAGNE
         F STENTON
         L KECSKES
         D SNOHA
         M PEPI
         S GRENDAHL
         D HELFRITCH
         K CHO
         D STRAND
       AMSRL WM T
         T B BURNS
         T WRIGHT

       AMSRL WM TA
         W BRUCHEY
         M BURKINS
         W GILLICH
         W GOOCH
         T HAVEL
         D HACKBARTH
         E HORWATH
         Y HUANG
         D KLEPONIS
         H MEYER
         M NORMANDIA
         J RUNYEON
         M ZOLTOSKI
       AMSRL WM TC
         R COATES
         K KIMSEY
         M LAMPSON
         L MAGNESS
         D SCHEFFLER
         G SILSBY
         R SUMMERS
         W WALTERS
       AMSRL WM TD
         J BARB
         D DANDEKAR
         A DIETRICH
         T FARRAND
         K FRANK
         N GNIAZDOWSKI
         F GREGORY
         A GUPTA
         T HADUCH
         T MOYNIHAN
         D PRITCHARD
         M RAFTENBERG
         E RAPACKI
         N RUPERT (10 CPS)
         M SCHEIDLER
         S SCHOENFELD
         S SEGLETES
         T WEERASOORIYA
       AMSRL WM TE
         A NIILER

45

NO. OF COPIES	ORGANIZATION	NO. OF COPIES	ORGANIZATION
1	DEFENCE RSH ESTAB VALCARTIER ARMAMENTS DIVISION R DELAGRAVE 2459 PIE X1 BLVD N PO BOX 8800 CORCELETTE QUEBEC GOA 1RO CANADA	4	FRANHOFER INSTITUT FÜR KURZZEITDYNAMIK ERNST MACH INSTITUT V HOHLER E STRASSBURGER R THAM K THOMA ECKERSTRASSE 4 D 79 104 FREIBURG GERMANY
5	DEUTSCH FRANZÖSISCHES FORSCHUNGSINSTITUT ST LOUIS H ERNST K HOOG H LERR T WOLF R NUSING CÉDEX 5 RUE DU GÉNÉRAL CASSAGNOU F 68301 SAINT LOUIS FRANCE	3	FRANHOFER INSTITUT FÜR KURZZEITDYNAMIK ERNST MACH INSTITUT K WEIMANN H SENF E STRASSBURGER AM KLINGELBERG 1 D 79588 EFRINGEN KIRCHEN GERMANY
1	DIEHL GMBH AND CO M SCHILDKNECHT FISCHBACHSTRASSE 16 D 90552 RÖTBENBACH AD PEGNITZ GERMANY	1	MINISTRY OF DEFENCE DGA SPART C CANNAVO 10 PLACE GEORGES CLEMENCEAU BP19 F 92211 SAINT CLOUD CÉDEX FRANCE
1	DYNAMEC RSCH AB Å PERSSON PO BOX 201 S 151 23 SÖDERTÄLJE SWEDEN	2	HIGH ENERGY DENSITY RSCH CTR V FORTOV G KANEL IZHORSKAYA STR 13 19 MOSCOW 127412 RUSSIAN REPUBLIC
3	ETBS DSTI P BARNIER M SALLES B GAILLY ROUTE DE GUERAY BOITE POSTALE 712 18015 BOURGES CEDEX FRANCE	1	INGENIEURBÜRO DEISENROTH F DEISENROTH AUF DE HARDT 33 35 D 5204 LOHMAR 1 GERMANY
2	FEDERAL MINISTRY OF DEFENCE DIR OF EQPT & TECH LAND RÜV 2 D HAUG L REPPER POSTFACH 1328 53003 BONN GERMANY	1	INST OF CHEMICAL PHYSICS S RAZORENOV 142432 CHERNOGOLOVKA MOSCOW REGION RUSSIAN REPUBLIC

NO. OF COPIES	ORGANIZATION	NO. OF COPIES	ORGANIZATION
7	INST FOR PROBLEMS IN MATERIALS SCIENCE S FIRSTOV B GALANOV O GRIGORIEV V KARTUZOV V KOVTUN Y MILMAN V TREFILOV 3 KRHYZHANOVSKY STR 252142 KIEV 142 UKRAINE	2	NATL DEFENCE HEADQUARTERS M PACEY PMO MRCV A HODAK PMO LAV OTTAWA ONTARIO KIA OK2 CANADA
1	INST FOR PROBLEMS OF STRESS G STEPANOV TIMIRYAZEVSKAYA STR 2 252014 KIEV UKRAINE	1	OTO BREDA M GUALCO VIA VALDIOCCHI 15 I 19136 LA SPEZIA ITALY
3	INST OF MECH ENGINEERING PROBLEMS V BULATOV D INDEITSEV Y MESCHERYAKOV BOLSHOY 61 VO ST PETERSBURG 199178 RUSSIAN REPUBLIC	5	RAPHAEL BALLISTICS CENTER M MAYSELESS Y PARTOM G ROSENBERG Z ROSENBERG Y YESHURUN BOX 2250 HAIFA 31021 ISRAEL
2	IOFFE PHYSICO TECH INST E DROBYSHEVSKI A KOZHUSHKO ST PETERSBURG 194021 RUSSIAN REPUBLIC	1	RSCH INST OF MECHANICS NIZHNIY NOVGOROD STATE UNIV A SADYRIN PR GAYARINA 23 KORP6 NIZHNIY NOVGOROD 603600 RUSSIAN REPUBLIC
1	K&W THUN W LANZ ALLMENDSSTRASSE 86 CH 3602 THUN SWITZERLAND	1	ROYAL NETHERLANDS ARMY J HOENEVELD V D BURCHLAAN 31 PO BOX 90822 2509 LS THE HAGUE NETHERLANDS
1	R OGORKIEWICZ 18 TEMPLE SHEEN LONDON SW 14 7RP UNITED KINGDOM	1	DEFENCE MATERIEL ADMIN WEAPONS DIRECTORATE A BERG S 11588 STOCKHOLM SWEDEN
1	MAX PLANCK INSTITUT FUR EISENFORSCHUNG GMBH C DERDER MAX PLANCK STRASSE 1 40237 DUSSELDORF GERMANY	2	SWEDISH DEFENCE RSCH ESTAB DIVISION OF MATERIALS S J SAVAGE J ERIKSON S 172 90 STOCKHOLM SWEDEN

NO. OF COPIES	ORGANIZATION	NO. OF COPIES	ORGANIZATION
3	SWEDISH DEFENCE RSCH ESTAB L HOLMBERG B JANZON I MELLGARD BOX 551 S 147 25 TUMBA SWEDEN	2	DERA FT HALSTEAD I CULLIS D SCOTT SEVENOAKS KENT TN14 7BP UNITED KINGDOM
1	TECHNION INST OF TECH FACULTY OF MECH ENGR S BODNER TECHNION CITY HAIFA 32000 ISRAEL	1	ERNST MACH INSTITUT R HEISER AM KLINGELBERG 1 D 79588 EFRINGEN KIRCHEN GERMANY
3	TECHNISCHE UNIVERSITÄT CHEMNITZ ZWICKAU A SCHROEDTER L KRUEGER L MEYER POSTFACH D 09107 CHEMNITZ GERMANY	1	TACHKEMONY ST 6 E HIRSCH NETANYA 42611 ISRAEL
2	TNO PRINS MAURITS LAB H PESKES R IJSSELSTEIN LANGE KLEIWEG 137 PO BOX 45 2280 AA RIJSWIJK THE NETHERLANDS	1	DEFENCE PROCUREMENT AGENCY (GR) I CREWTHER WEAPONS AND AMMO DIV FEUERWERKERSTRASSE 39 CH 3602 THUN SWITZERLAND
1	MONASH UNIVERSITY DEPT OF CIVIL ENG R GRZEBIETA CLAYTON VICTORIA 3168 AUSTRALIA	1	DEFENCE RESEARCH ESTAB VALCARTIER A DUPUIS 2459 BLVD PIE XI NORTH VAL BELAIR QUEBEC GEJ 1X5 CANADA
6	CENTRE DE RECHERCHES ET D'ETUDES D'ARCUEIL D BOUVART C COTTENNOT S JONNEAUX H ORSINI S SERROR F TARDIVAL 16 BIS AVENUE PRIEUR DE LA CÔTE D'OR F 94114 ARCUEIL CÉDEX FRANCE	1	CRANFIELD UNIVERSITY HEAD BALLISTICS GROUP A B CROWLEY RMCS SHRIVENHAM SWINDON SN6 8LA UNITED KINGDOM
		3	FRENCH GERMAN RSCH INST D HENSEL M GIRAUD G KRAUTH 5 RUE DU GENERAL CASSAGNOU BOITE POSTALE 34 F 68301 SAINT LOUIS CEDEX FRANCE

NO. OF COPIES	ORGANIZATION	NO. OF COPIES	ORGANIZATION
2	SABO ARMSCOR COMBAT SPT P NEL L DU PLESSIS G KRAUTH PRIVATE BAG X337 0001 PRETORIA REPUBLIC OF SOUTH AFRICA	1	DIRECTOR UNIVERSIDAD POLITECNICA V SANCHEZ-GALVEZ ETSI CAMINOS UPM CIUDAD UNIVERSITARIA MADRID 28040 SPAIN
1	RIMAT ADVANCED TECHNOLOGIES LTD M RAVID 8 B SIMATAT HAYEREK HOD HASHARON 45264 ISRAEL	1	RUSS ACADEMY OF ROCKET AND ARTILLERY SCIENCE V SOLOVIEV GOSPITALITY LANE 10 107564 MOSCOW RUSSIA
1	TNO DEFENCE RESEARCH H PASMAN POSTBUS 6006 2600 JA DELFT THE NETHERLANDS	2	CSIRO MANUFACTURING SCI AND TECH R G ODONNELL A STEVENSON PRIVATE BAG 33 CLAYTON SOUTH VICTORIA 3169 AUSTRALIA
2	DSTO WEAPONS SYS DIV A WILDEGGER GAISSN N BURMAN RLLWS PO BOX 1500 SALISBURY SA 5108 AUSTRALIA	1	DERA STRUCTURAL MATERIALS CTR GRIFFITH BLDG A 7 R A SMITH FARNBOROUGH HAMPSHIRE GU14 OLX UNITED KINGDOM
1	ECOLE ROYAL MILITAIRE E CELENS AVENUE DE LA RENAISSANCE 30 1000 BRUXELLE BELGIQUE		
1	A STILP BUSSARDWEG 7 79110 FREIBURG GERMANY		
1	G A SCHROEDER IN DEN GATTERN 3 79594 INZLINGEN GERMANY		
1	DEFENCE RES & DEV ORG P U DESHPANDE MINISTRY OF DEFENCE 316 B WING SENA BHAVAN NEW DELHI 110 011 INDIA		

REPORT DOCUMENTATION PAGE

1. AGENCY USE ONLY *(Leave blank)*	2. REPORT DATE	3. REPORT TYPE AND DATES COVERED
	November 2001	Final, October 1999–September 2000

4. TITLE AND SUBTITLE
Damage Assessment in TiB_2 Ceramic Armor Targets

5. FUNDING NUMBERS
N/A

6. AUTHOR(S)
Nevin L. Rupert, William H. Green, Joseph M. Wells, and Kevin J. Doherty

7. PERFORMING ORGANIZATION NAME(S) AND ADDRESS(ES)
U.S. Army Research Laboratory
ATTN: AMSRL-WM-TD
Aberdeen Proving Ground, MD 21005-5066

8. PERFORMING ORGANIZATION REPORT NUMBER
ARL-TR-2607

9. SPONSORING/MONITORING AGENCY NAMES(S) AND ADDRESS(ES)

10. SPONSORING/MONITORING AGENCY REPORT NUMBER

11. SUPPLEMENTARY NOTES

12a. DISTRIBUTION/AVAILABILITY STATEMENT
Approved for public release; distribution is unlimited.

12b. DISTRIBUTION CODE

13. ABSTRACT*(Maximum 200 words)*

The interaction between long rods and ceramics is only partially understood; however, this understanding is essential in the design of improved performance of impact-resistant materials and armor system design applications. The current work takes a preliminary look into the modern mythology surrounding the formation of radial cracking in ceramics during ballistic penetration. Tests were conducted using a 32-g tungsten alloy laboratory penetrator with a length to diameter ratio (L/D) = 20 at a nominal impact velocity of 1,600 m/s. Testing evaluated both prestressed and unstressed titanium diboride (TiB_2) ceramic tiles. Evaluation of the damage included microstructural analysis using a scanning electron microscope (SEM) with a Robinson backscatter detector for surface structure, the x-ray computed tomography (CT) nondestructive technique to completely scan the interior of each disk, and limited analytical modeling of the stress state.

14. SUBJECT TERMS
ceramic, armor, mesocracking, computed tomography, SEM, interface defeat, analytical modeling

15. NUMBER OF PAGES
59

16. PRICE CODE

17. SECURITY CLASSIFICATION OF REPORT	18. SECURITY CLASSIFICATION OF THIS PAGE	19. SECURITY CLASSIFICATION OF ABSTRACT	20. LIMITATION OF ABSTRACT
UNCLASSIFIED	UNCLASSIFIED	UNCLASSIFIED	UL

INTENTIONALLY LEFT BLANK.